

AD-A107 867

ARIZONA STATE UNIV TEMPE CENTER FOR SOLID STATE SCIENCE
SULFUR IN THE CORROSION OF SUPERALLOYS.(U)
NOV 81 J B WAGNER

F/G 11/6

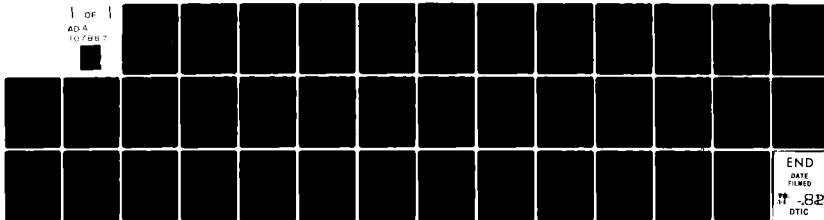
DAA629-80-C-0049

UNCLASSIFIED

ARO-14925.2-MS

NL

1 OF 1
AD-A
107867



END
DATE
FILMED
11-82
DTIC

SECRET

(3)

(12)

SECURITY CLASSIFICATION OF THIS PAGE (When Data Entered)

REPORT DOCUMENTATION PAGE		READ INSTRUCTIONS BEFORE COMPLETING FORM
1. REPORT NUMBER 14925.2-MS	2. GOVT ACCESSION NO. AD-A107867	3. REPORTS CATALOG NUMBER
4. TITLE (and Subtitle) Sulfur in the Corrosion of Superalloys		5. TYPE OF REPORT & PERIOD COVERED Final Report: 10 Dec 77 - 15 Jul 81
		6. PERFORMING ORG. REPORT NUMBER
7. AUTHOR(s) J. Bruce Wagner, Jr.		8. CONTRACT OR GRANT NUMBER(s) DAAG29 78 G 0032; DAAG29 80 C 0049
9. PERFORMING ORGANIZATION NAME AND ADDRESS Arizona State University Center for Solid State Science Tempe, AZ 85287		10. PROGRAM ELEMENT, PROJECT, TASK AREA & WORK UNIT NUMBERS
11. CONTROLLING OFFICE NAME AND ADDRESS U. S. Army Research Office Post Office Box 12211 Research Triangle Park, NC 27709		12. REPORT DATE 6 Nov 81
		13. NUMBER OF PAGES 29
14. MONITORING AGENCY NAME & ADDRESS (if different from Controlling Office) Dr. G. Max Irving Admin. Contracting Officer Office of Naval Research Resident Rep. Bandolier Hall West-Room 204 University of New Mexico, Albuquerque, NM 87131		15. SECURITY CLASS. (of this report) Unclassified
16. DISTRIBUTION STATEMENT (for this Report) Approved for public release; distribution unlimited.		15a. DECLASSIFICATION/DOWNGRADING SCHEDULE
17. DISTRIBUTION STATEMENT (of the abstract entered in Block 20, if different from Report) NA		
18. SUPPLEMENTARY NOTES The view, opinions, and/or findings contained in this report are those of the author(s) and should not be construed as an official Department of the Army position, policy, or decision, unless so designated by other documentation.		
19. KEY WORDS (Continue on reverse side if necessary and identify by block number) high temperature corrosion impurity diffusion sulfidation		
20. ABSTRACT (Continue on reverse side if necessary and identify by block number) See Page 5.		

NOV 27 1981

A

81 11 24 072

AD A107867

DTIC FILE COPY

THE VIEW, OPINIONS, AND/OR FINDINGS CONTAINED IN THIS REPORT ARE THOSE OF THE AUTHOR AND SHOULD NOT BE CONSTRUED AS AN OFFICIAL DEPARTMENT OF THE ARMY POSITION, POLICY, OR DECISION, UNLESS SO DESIGNATED BY OTHER DOCUMENTATION.

FORWARD

In energy systems, the problems associated with high temperature corrosion especially in mixed oxidants, e.g. oxygen containing sulfur dioxide and sulfur trioxide, have in many instances limited the use of certain materials. As an example of the drastic changes in reaction rate, the oxidation rate of nickel in oxygen plus some sulfur containing gas may exceed the rate in pure oxygen by as much as 10^6 ! Accordingly research to determine diffusivity of sulfur through oxides was undertaken along with a parallel study on the kinetics of corrosion of nickel in $\text{SO}_2\text{-O}_2$ gas mixtures.

STATEMENT OF THE PROBLEM

Many high temperature corrosion processes are determined by the rate at which an impurity anion (not oxygen) is transported through a corrosion product layer. An example is the high temperature corrosion of metals and alloys in mixed oxidants such as $\text{SO}_2\text{-O}_2$ gas mixtures. Accordingly, research was initiated in (1) Corrosion of nickel in $\text{SO}_2\text{-O}_2$ gas mixtures at 800° . (2) Defect structure of calcia and of yttria stabilized zirconia; and diffusion of radiotracer sulfur-35 and tellurium 127m in calcia stabilized zirconia. The tracer studies bear directly on the problem of sulfur penetration into chemical sensor materials and also the penetration of sulfur through thermal barrier layers of zirconia on turbine blade alloys.

ABSTRACT

This study was divided into three interrelated sections. These were (1) corrosion of nickel in $\text{SO}_2\text{-O}_2\text{-Ar}$ gas mixtures at 800°C ; (2) defect structure of calcia and of yttria stabilized zirconia; and (3) diffusion of radio-tracer sulfur-35 and of tellurium 127m in calcia stabilized zirconia. The corrosion study resulted in a confirmation of linear kinetics for corrosion of nickel in $\text{SO}_2\text{-Argon}$ gas mixtures at 800°C and an agreement of a self-consistent mechanism involving the migration of SO_2 as a gas molecule through the outer NiO layer and dissociation at the inner sulfide layer as a rate determining step. The corrosion kinetics in 20% O_2 -variable SO_2 -balance argon and in 30% SO_2 variable O_2 -balance argon were extremely rapid. These data did not show that interconnected stringers of sulfide through the outer NiO layer was responsible for the observed kinetics.

The ionic conductivity and diffusion in calcia stabilized zirconia, in yttria stabilized zirconia and related structures, were developed using a theoretical model which when fitted to the existing experimental data yielded good agreement. Briefly, the increase in conductivity with dopant concentration followed by a maximum and a subsequent decrease in conductivity was explained by considering jumps of oxygen via oxygen vacancies one-fold and two-fold coordinated calcium (or other aliovalent dopants) in the zirconia.

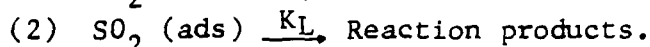
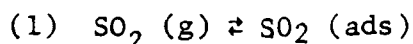
Radiotracer sulfur-35 or tellurium-127m was diffused into 15 m/o CaO-ZrO_2 (CSZ). A multimode diffusion process was observed. The two bulk diffusion processes were related to jumps via anion vacancies in the CSZ. Surprisingly, there was little or no correlation between size or mass in these studies, i.e. sulfur and tellurium both diffused at approximately the same rate. The diffusivities were about four orders of magnitude greater than sulfur in NiO in agreement with the large vacancy concentrations in CSZ. Furthermore, both sulfur and tellurium diffused more slowly than oxygen but faster than either Ca or Zr in CSZ.

1. Corrosion of nickel in SO_2 - O_2 -Ar Gas mixtures at 800°C .

Polycrystalline nickel samples (99.6 + w/o) approximately 25 by 17 and 0.5mm were polished mechanically on SiC paper from 240 grit to 600 grit. Some samples were pre-annealed in one atmosphere of hydrogen at about 800°C prior to the experiment. In addition, a few experiments were carried out on single crystals of nickel (99.99 + w/o). Results were the same as for polycrystalline samples. Mixtures of SO_2 - O_2 -Ar were obtained using metered capillary flowmeters. The gas mixtures are indicated on the stability diagram in Fig. 1. Kinetics were determined using an Ainsworth automatic recording balance. Preliminary experiments were performed on nickel in pure oxygen to test for self consistent data. See Fig. 2.

A. Corrosion in SO_2 -Argon gas mixtures.

At 800°C , the kinetics in SO_2 -Ar gas mixtures were linear. See Fig. 3. These data are in good agreement with the data of Nakai and Takazawa (1) and those of Kofstad and Akesson (2). See Fig. 4. According to (2), the rate determining step is



Our data are in accord with their suggestion. A suggested mechanism along with calculated activities and partial pressures are shown in Fig. 5. Markers were always found at the sulfide-oxide interface corrosion.

B. Corrosion in 20% O_2 - variable SO_2 -balance Ar. at 800°C .

These kinetics exhibited protective behavior at $\leq 20\%$ SO_2 and were exceedingly rapid at $\geq 30\%$ SO_2 . See Fig. 6. The drastic change in kinetics suggest a change in mechanism. We tested the resistance of the scale of nickel sulfide containing some sulfide. In no case did we find evidence by electrical measurements nor by optical and SEM metallographic examination of stringers of sulfide forming a continuous path through the NiO scale as was reported by Luthra and Worrell (3,4) for similar corrosion at 603°C .

In both the cases of SO_2 -Ar and 20% O_2 -variable SO_2 -balance Ar, both the inner layer of sulfide and the outer layer of NiO (containing sulfur but no continuous stringers) increase in thickness with time. See Fig. 7. We are currently studying the conductivity of Ni_3S_2 - NiO two phase mixtures contribute to an understanding of these phenomena. (5).

C. Corrosion in 30% SO₂-variable O₂-balance Ar.

Initially as the oxygen content is increased (2%, 5%, 10%) the kinetics decrease. However, for $\geq 20\%$, the kinetics increase drastically. See Fig. 8. At the higher values of P_{O₂}, NiSO₄ formed on the outer surface of the NiO layer in accord with the stability diagram. See Fig. 1. Moreover, the markers were found at the inner sulfide layer-outer nickel oxide layer interface as in in the study mentioned above. However, at lower oxygen pressures, the markers were found in the middle of the outer oxide layer.

D. Effect of pre-oxidation on corrosion mechanism.

Clearly the transport of SO₂ or sulfur in some form through the corrosion product affects the kinetics dramatically. Accordingly, nickel coupons were oxidized in pure oxygen and then exposed to sulfur containing gases. See Fig. 9. There is a relation between the thickness of pre-formed NiO and the incubation period or onset of rapid kinetics after admitting SO₂ gases. However, the relation is not incubation period proportional to the square of the pre-formed oxide thickness as one would expect.

2. Defect Structure, Ionic Conductivity and Diffusion in Calcia-, in Yttria-stabilized Zirconia and in related Fluorite structures.

Prior to studying the diffusion of radio tracer S-35 and Te-127m in CaO-ZrO_2 , a detailed theoretical analysis was performed on the existing data for ionic conductivity of calcia-, or yttria-stabilized zirconia and other related fluorites. In the case of the stabilized zirconias, the isothermal ionic conductivity first increases with added aliovalent dopant, attains a maximum and then decreases. See Appendix, especially Fig. 1. While it is well-known that oxygen migrates via vacancies in these materials, the occurrence of a maximum and subsequent decrease was not well explained. When the concentration of dopant attains 12-13m/o (CaO-ZrO_2) and 8-9 m/o ($\text{Y}_2\text{O}_3\text{-ZrO}_2$), the anion vacancies are not in dilute solution. The vacancies and dopant atoms form dopant-defect associates. The ionic conduction was assumed to occur via a multimode mechanism through and between Ca^{2+} -one fold and Ca^{2+} -two fold coordinated anion vacancy sites. This model was successfully applied to calcia stabilized zirconia (See Appendix 1). A similar analysis has been applied to yttria stabilized zirconia. Results of the theory and experimental data are shown in Fig. 10.

Furthermore, the theoretical model is also applicable to various other oxide electrolyte systems with the fluorite structure, such as the rare oxides (Me_2O_3) - stabilized zirconia with general formula $\text{Me}_{4x} \text{Zr}_{1-4x} \text{O}_{2-2x}$ ($\text{Me} = \text{Y, Ta, Dy, Sc, Yb, Sm, Ho, In}$) and also CaO - and Me_2O_3 - doped CeO_2 and ThO_2 systems. A manuscript is in preparation describing these results.

3. Radiotracer Diffusion of S-35 and Te-127m in Calcia-stabilized Zirconia and Yttria-stabilized Zirconia.

Polycrystalline samples of calcia stabilized zirconia, (9, 13, 15 and 18 m/o) were obtained from the General Electric Company courtesy D. Chatterji and K. Lay. Polycrystalline samples of CSZ of 15 m/o calcia were obtained from the Zircoa Corporation. Yttria-stabilized zirconia polycrystalline samples were obtained from Viking Chemical courtesy of Dr. M. Kleitz of Grenoble and single crystalline YSZ (9.6 m/o) was obtained from Dr. Joseph Wenckus, President of Ceres Corporation. In some experiments the samples were used as-received while in others the samples were given a high temperature anneal prior to the diffusion anneal. The experimental procedure was almost the same as that for sulfur diffusion in single crystalline NiO. [(Ref.12)]. Supported by ARO under DAAG-29-76-G-0196 and DAH C04-74-G-0130]. Cylindrical pellets, about 11 mm in diameter by 1.7 mm thick were used as received or pre-annealed in 1 atm O₂. The samples were polished on two flat faces using SiC paper and diamond paste of 1 micron. The ionic conductivity of these samples was first checked to ascertain that the material behaved in accord with previous studies.

The radiotracer (S-35 in benzene or Te-127m in 4m HCl) was deposited in a Pt crucible by slowly evaporating the solvents. The Pt crucible and the sample were encapsulated in a quartz tube and the tube given diffusion anneal (850°C to 1250°C for 0.5 to 300 hrs. depending on the temperature). The tubes were quenched, samples removed and washed in acetone or toluene. The cylindrical sides were ground away $\sim 5\sqrt{DT}$ to avoid side effects.

The tracer penetration profiles were obtained by counting the weak betas and serially sectioning the samples. The thicknesses removed were obtained by weight change. A high surface activity ($10^5 - 10^6$ cpm) was used so corrections for coincidence loss were made. No corrections for self absorption were made because of the deep penetrations and weak beta energies.

The penetration profiles for S-35 and Te-127m in 15 m/o CaO-ZrO₂ generally consisted of four regions: These were:

- I. Near surface region ($\Delta x < 5\mu$ at 1000°C) where a sharp drop in activity is observed.
- II. A first intermediate region which corresponds to the diffusion process with the slower diffusivity and higher solubility.
- III. A second intermediate range which corresponds to the diffusion process with high diffusivity and low solubility.
- IV. A short-circuit diffusion and/or almost constant activity region which is characterized by a long "diffusion tail" with much scatter in activity for a given penetration distance.

Fig. 10 shows a typical penetration profile of S-35 and Te-127m in 15 m/o CaO-ZrO₂. Region I may be related to a surface process. No analysis of this narrow region was performed. Regions II and III appear to be bulk diffusion processes and region IV a short circuit process or processes. The data for Regions II and III were analyzed analogously to similar data for NiO (12) and an Arrhenius plot is shown in Fig. 11.

Because we used polycrystalline samples, we checked the $t^{1/2}$ dependence of the profiles for various diffusion times (1.5, 6.0 and 24 hrs at 1000°C). Regardless of the diffusion anneal time, all profiles showed well defined Regions II and III and coincidence with one another. We conclude that Regions II and III are bulk diffusion controlled.

Several important points can be made. These are:

- (1) Sulfur and tellurium exhibit virtually identical diffusion coefficients in both modes (Regions II and III), i.e. both sulfur and tellurium exhibit the same slower and faster diffusivities, D_s and D_f , and we find no appreciable size effect [$O^{2-}=1.32 \text{ \AA}$, $S^{2-}=1.84 \text{ \AA}$, $Te^{2-}=2.11 \text{ \AA}$] or mass effect [O 18, S 35, Te 127].
- (2) Both modes of sulfur and tellurium diffusion, D_s and D_f , exhibit two distinct regions in the temperature dependence (See Fig. 11). At the higher temperatures ($1050^\circ\text{C} \leq T \leq 1250^\circ\text{C}$) both modes have very small temperatures ($\sim 10 \text{ kcal/mole.}$) In the lower temperature range ($850^\circ\text{C} \leq T \leq 1050^\circ\text{C}$) both modes are very temperature dependent. The Arrhenius equations for their diffusivities in cm^2/sec are

$$850^\circ\text{C} \leq T \leq 1050^\circ\text{C}; D_s = 1.995 \times 10^3 \exp \left[\frac{-80.08 \text{ kcal/mol}}{RT} \right];$$

$$D_f = 6.84 \times 10^8 \exp \left[\frac{-103.65 \text{ kcal/mol}}{RT} \right];$$

$$1050^\circ\text{C} \leq T \leq 1125^\circ\text{C};$$

$$D_s = 3.55 \times 10^{-9} \exp \left[\frac{-7.32 \text{ kcal/mol}}{RT} \right];$$

$$D_f = 3.09 \times 10^{-7} \exp \left[\frac{-10.25 \text{ kcal/mol}}{RT} \right];$$

The absolute magnitudes of D_s and D_f for S-35 and Te-127 are almost four orders of magnitude faster than S-35 in NiO reported by Hwang and Wagner (12). This result is in general agreement with the much higher concentration of oxygen vacancies in CSZ than in NiO. The values of D_s and D_f are less than the diffusivity of oxygen in CSZ but greater than the diffusivities of Ca and Zr.

Similar experiments were carried out for S-35 in yttria-stabilized zirconia, both polycrystalline pellets (9 m/o) and single crystals (9.6 m/o). In these studies at 1000°, 1100° and 1200°C both the solubility of sulfur and the diffusion coefficients were extremely small. Single and polycrystalline samples yielded the same values for diffusivity and evidence for multimode diffusion was not obtained because of the extremely small penetration profiles. Approximate values were:

$$D(S \rightarrow YSZ) \cong 8.68 \times 10^{-14} \text{ cm}^2 \text{ sec}^{-1} (1200^\circ\text{C})$$

$$\cong 1.16 \times 10^{-14} \text{ cm}^2 \text{ sec}^{-1} (1100^\circ\text{C})$$

$$\cong 3.78 \times 10^{-15} \text{ cm}^2 \text{ sec}^{-1} (1000^\circ\text{C})$$

In related experiments, the diffusivity of sulfur-35 was determined in CSZ as a function of calcia content. Samples of 9, 13, 15 and 18 m/o CaO were kindly furnished by D. Chatterji and K. Lay of the General Electric Company.

In contrast to the data on commercially available 15 m/o CaO-ZrO₂ from Zircoa, the results on the GE material depended markedly on the time of the pre-diffusion anneal. The higher the pre-diffusion anneal temperature and longer the pre-diffusion anneal time, the smaller was the observed sulfur solubility and the smaller were the diffusivities. The diffusion profiles so obtained did not follow the expected $t^{1/2}$ dependence. Curiously, the electrical conductivity showed no effects of "aging" above 1100°C. We continue to analyze these data.

BIBLIOGRAPHY

1. H. Nakai and H. Takazawa,
Nippon Kinzoku Gakkaishi 40 466 (1976).
2. P. Kofstad and G. Åkesson, Oxidation of Metals
12 No. 6, 503 (1978).
3. K.L. Luthra and W.L. Worrell, Trans. Met.
Soc. 9A 1055 (1978).
4. K.L. Luthra and W.L. Worrell, Trans. Met.
Soc. 10A 621 (1979).
5. V.B. Tare and J.B. Wagner, Jr.
Research-in-progress, Center for Solid State Science,
Arizona State University.
6. J.M. Dixon, L.D. LaGrange, U. Merten,
C.F. Miller and J.T. Porter II, J. Elec-
trochem. Soc. 110 276 (1963).
7. D.W. Strickler and W.G. Carlson, J.
Am. Ceram. Soc. 47, 122 (1969).
8. D.W. Strickler and W.G. Carlson,
ibid. 48 286 (1965).
9. J.E. Bauerle and J. Hrizo. J.
Phys. Chem. Solids 30, 565 (1969).
10. R.E.W. Casselton, Phys. Status Solidi
A2 571 (1970).
11. A.I. Ioffe, D.S. Ruthman and
S.V. Karpachou, Electrochimica
Acta 23 141 (1978).
12. W.Y. Howng and J.B. Wagner Jr.
J. Phys Chem. Solids 19 1019 (1978).

Scientific Personnel

J. Bruce Wagner, Jr., Professor/Director Center for Solid State Science, ASU

Dr. Akio Nakamura, Faculty Research Associate

Dr. Keshawa Shahi, Faculty Research Associate

Mr. Ashok Khandkar, Graduate Student, Engineering Science

Mr. Haruyoshi Yagi, Graduate Research Associate
(Writing PhD Thesis-to be completed for May/82 Graduation)

APPENDIX 1.



Reprinted from JOURNAL OF THE ELECTROCHEMICAL SOCIETY
Vol. 127, No. 11, November 1980
Printed in U.S.A.
Copyright 1980

Defect Structure, Ionic Conductivity, and Diffusion in Calcia-Stabilized Zirconia

Akio Nakamura* and J. Bruce Wagner, Jr.*

Center for Solid State Science, Arizona State University, Tempe, Arizona 85281

ABSTRACT

A quantitative theoretical model which accounts for the variations of ionic conductivity of calcia-stabilized zirconia, $\text{Ca}_{2x}\text{Zr}_{1-2x}\text{O}_{3-2x}$, with oxygen vacancy concentration, x , and temperature, T , has been developed based on the consideration of effective anion-site coordination of effectively negatively charged calcium ion, Ca^{2+} . The theory extends the conventional concept of dopant-defect complexes (or associates) and demonstrates that ionic conduction in this system proceeds by a multimode mechanism through and between different degrees of dopant-defect associates. The primary mechanism is oxygen transport through the channel of onefold effectively Ca^{2+} coordinated anion sublattice, that is, oxygen vacancy $\text{V}_{\text{O}^{2-}}$ transport inside the onefold bonded ($\text{Ca}^{2+}\text{-V}_{\text{O}^{2-}}$) defect complex. The theory subsequently predicts the occurrence of a rather sharp maximum of ionic conductivity at oxygen vacancy concentration $x = 0.0625$ and reproduces the experimental isothermal $\log \sigma$ vs. x curves reported by various investigators quite satisfactorily. Accordingly, numbers of parameters which characterize the defect structure, the ionic conduction, and the diffusion process in this system are derived from the curve-fitting procedure of the theoretical expression for ionic conductivity with experimental ones.

It is now well recognized that zirconia stabilized in the cubic fluorite structure by substitution of aliovalent oxides, such as CaO , Y_2O_3 , and rare earth oxides, is essentially an oxide ion conductor with its high ionic conductivity due to high oxygen vacancy concentration introduced into the anion sublattice by these substitutions (1). Numerous experimental works on electrical conductivity on these systems have shown that ionic conductivity of these systems exhibits a maximum value around the minimum dopant level required to stabilize the cubic fluorite phase at constant temperature. For example, in CaO -stabilized zirconia, $\text{Ca}_{2x}\text{Zr}_{1-2x}\text{O}_{3-2x}$, the maximum occurs around 12-13 mole percent (m/o) CaO content (2-5) ($x = 0.060\text{-}0.065$) and in the Y_2O_3 -stabilized zirconia, $\text{Y}_{4x}\text{Zr}_{1-4x}\text{O}_{2-2x}$, around 8-9 m/o Y_2O_3 content (2, 4, 6) ($x = 0.037\text{-}0.041$). At higher concentrations within the cubic fluorite phase regions, the ionic conductivity decreases with increasing dopant content. The activation energy for ionic conduction is also reported to increase with increasing dopant content (4, 5). Similar behavior is also reported in the other fluorite oxide systems, i.e., ThO_2 (7) and CeO_2 (8) based solid electrolytes, where,

since pure thorium and ceria have cubic fluorite structure, dopants such as CaO and Y_2O_3 are used only to introduce the extrinsic oxygen vacancies into the anion sublattice. This decrease in ionic conductivity with increasing vacancy concentration has been qualitatively regarded as the result of vacancy ordering (5) vacancy clustering (9), or dopant-vacancy association (10) in the higher oxygen vacancy concentration range.

Recently, several attempts to explain this behavior have been undertaken: O'Keeffe (11) and Barker and Knop (12) have shown that when vacancy-vacancy repulsive interaction is so strong that the numbers of the first and the second nearest neighbor vacancy-vacancy configurations are prohibited, the maximum in ionic conductivity shifts to the lower vacancy concentration ranges than that expected from the usual hopping model in which $\sigma \propto x(1-x)$, so that σ_{max} is expected at $x = 0.5$. Casselton (6) for the $\text{Y}_2\text{O}_3\text{-ZrO}_2$ system and Hammou (13) for the $\text{Y}_2\text{O}_3\text{-ThO}_2$ system, respectively, proposed models to explain this behavior using the extended Lidiard model (14) which is based on the presence of dopant-vacancy complexes and Debye-Hückel type interactions. Hammou also tested Barker's model mentioned above. None of these models resulted in quantitative agreement with experimental data.

* Electrochemical Society Active Member.

Key words: electrolyte, conductance, transport.

Most recently, Schmalzried (15) interpreted these phenomena under the assumptions of (i) Debye-Hückel type electrostatic interaction for low defect concentration range and (ii) ordering of oppositely charged defects for high defect concentration range, neglecting the formation of defect associates. Schmalzried showed that these assumptions lead to a decrease of the correlation factor of defects with increasing defect concentration and also to an increase in the activation energy for defect motion in a qualitative manner. Judging from the preceding brief literature survey, there seems to exist no theoretical model which accounts for the phenomena in these systems in a quantitative manner. Accordingly, the aim of the present paper is to propose an alternative theoretical model to serve this purpose by choosing calcia-stabilized zirconia as a representative system.

In the next section, a brief survey of the ionic conductivity data of calcia-stabilized zirconia reported in literature is given, and in the subsequent section the theoretical model is described.

Ionic Conductivity Data of Calcia-Stabilized Zirconia, $\text{Ca}_{1-x}\text{Zr}_{1+x}\text{O}_{2-x}$ System

Figure 1 shows the isothermal $\log \sigma$ vs. oxygen vacancy concentration x plots at $T = 600^\circ\text{C}$, 800°C , 1000°C , 1200°C , and 1400°C reported in literature. Included are data only by the authors who studied σ as a function of dopant content in a systematic manner.

The data of Stricker and Carlson (2), Tien (3), Dixon et al. (4), and Tien and Subbarao (5) all agree that the stability region of the cubic fluorite phase extends from around 12-13 m/o CaO to around 20-22 m/o CaO at temperatures between approximately 800°C and 1400°C . Furthermore, the conductivity maximum exists inside the cubic fluorite phase near the monoclinic-cubic solid solution phase boundary, i.e., at 12-13 m/o CaO content ($x = 0.060$ - 0.065). In contrast, Carter and Roth (16) report that the stability region extends from about 10 to 19 m/o CaO at 1400°C and their data seem to show the tendency that the conductivity maximum shifts from around 13 m/o CaO at 1000°C to 15 m/o CaO at 1400°C .

As is apparent from Fig. 1, the ionic conductivity of calcia-stabilized zirconia initially increases with oxygen vacancy concentration x , and reaches a maximum around 12-13 m/o CaO content ($x = 0.060$ - 0.065). The conductivity then decreases, initially rather sharply and then more slowly, with oxygen vacancy concentration x within the cubic fluorite phase region. The rate of decrease of ionic conductivity with x increases with decreasing temperature and the conductivity decreases by a factor of $\sim 1/20$ at 600°C when x increases from 0.065 to 0.100. This means that the activation energy for ionic conduction increases with x . Typical values are 26.2 kcal/mole for 13 m/o CaO and 31.1 kcal/mole for 20 m/o CaO (5).

Another interesting feature is the order-disorder transition. Subbarao et al. (5, 17) observed this phenomenon below 1000°C in samples with higher CaO content (18 and 20 m/o CaO). Some of these data, designated as "ordered," are also included in Fig. 1. "Ordered" samples at these compositions have a lower but finite conductivity which is converted to that of the "disordered" phase after heat-treatments at 1400°C . Carter and Roth (16) also examined this order-disorder phenomenon rather extensively. Their data indicate that below 1100°C , even in samples with low CaO content (13.2 and 14.2 m/o CaO), in some cases the resistivity changes by a factor of over 10, showing no tendency to saturate with time. The reason for this discrepancy between Subbarao et al. (5, 17) and Carter and Roth (16) is not clear at present, although it seems reasonable to assume from these observations that in samples with higher CaO content and at lower temperatures calcium ions Ca^{2+} and oxygen vacancies V_{O}^{2-} would order in some fashion which causes the

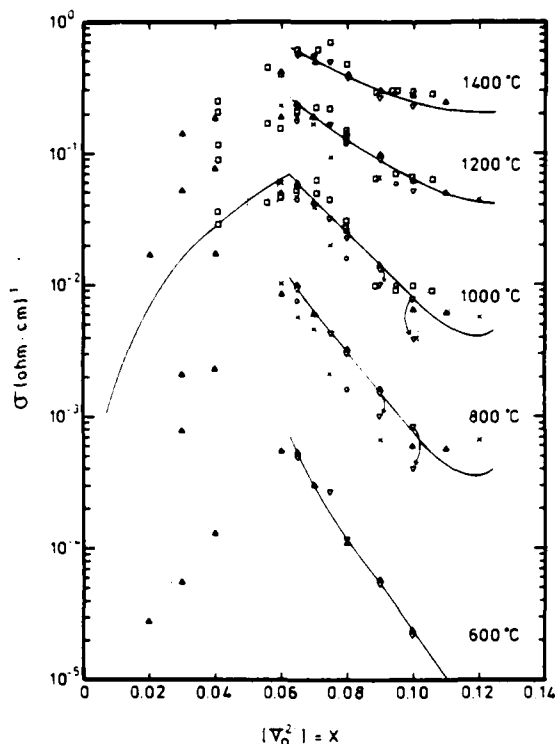


Fig. 1. Isothermal $\log \sigma$ vs. oxygen vacancy concentration x plots at 600°C , 800°C , 1000°C , 1200°C , and 1400°C .

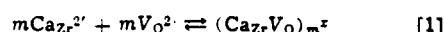
Experimental points	Reference number
○ Stricker and Carlson	(2)
▲ Tien	(3)
× Dixon, LaGrange, Merten, Miller and Porter	(4)
▽ Tien and Subbarao	(5)
□ Carter and Roth	(16)
— Theoretical curves according to Eq. [13] at $0.0625 \leq x \leq 0.125$ and Eq. [13] at $0 \leq x \leq 0.0625$, $T = 1000^\circ\text{C}$	
— The phase boundary of the cubic fluorite phase according to the above authors.	
▽ Lower values indicated by arrow. σ at ordered state according to Ref. (5) and (17).	

substantial decrease in ionic conductivity after prolonged heat-treatments.

Theoretical

The main aim of the theoretical model is to reproduce the experimental $\log \sigma$ vs. x curves shown in Fig. 1 over the entire temperature ranges in a quantitative manner consistent with the physical reality of the system. This includes the increase in activation energy for ionic conduction with x .

As far as the authors are aware, Kröger (10) was the first to suggest that ionic conduction and oxygen diffusion in calcia-stabilized zirconia (CSZ) probably occurs via migration of oxygen vacancies V_{O}^{2-} in $(\text{Ca}_{1-x}\text{Zr}_{1+x}\text{O}_{2-x})_{\text{m}}$. Kröger described this association process by a usual defect equilibrium equation



Applying the mass action law to the above equation and assuming electrostatic binding energy of the defect complex, Kröger concluded that most of the calcium (and therefore V_{O}^{2-}) is present as neutral calcium ion-oxygen vacancy pairs or clusters. This description corresponds in general form with the theory of Lidiard

for aliovalent impurity diffusion in alkali-halide systems (14). But when the impurity (dopant) concentration and therefore also the defect concentration becomes as high as in CSZ, these treatments do not appear to be valid. First, let us assume that oxygen and therefore $V_{O^{2-}}$ diffusion proceeds via defect complexes $(Ca^{2+}V_{O^{2-}})^{\times}$ ($m = 1$ in Eq. [1]). In the fluorite structure, since every cation has 8-first, 24-second, 24-third . . . nearest neighbor anion sites, all the anion sites will be just effectively onefold coordinated by dopant cations Ca^{2+} when the dopant concentration reaches $2x = 2/Z'$ for $Ca_{1-x}Zr_{1-x}O_{3-2x}$, i.e., in this case $Z' \cdot 2x = 2$, where Z' is the effective anion site coordination number of Ca^{2+} in this system. This means that at the composition $x = 1/Z'$, every $V_{O^{2-}}$ jump occurs inside $(Ca^{2+}V_{O^{2-}})^{\times}$ onefold effectively associated defect complexes. Therefore, conductivity should be a maximum. Beyond this composition the average effective Ca^{2+} coordination number to the anion sublattice becomes greater than 1, i.e., the number of density of 2-fold Ca^{2+} coordinated anion sites becomes an appreciable fraction of the total available jump sites; so the ionic conductivity should decrease, because the effective path for $V_{O^{2-}}$ migration through $(Ca^{2+}V_{O^{2-}})^{\times}$: 1-fold effectively Ca^{2+} associated defect complexes decreases. This is indeed the case for CSZ if we assume an effective anion site coordination number of Ca^{2+} : $Z' = 16$: the experimental observed ionic conductivity maximum occurs around $x = 0.060-0.065$, whereas the theoretically derived conductivity maximum is expected at $x = 1/Z' = 1/16 = 0.0625$. If only the first nearest neighbor $Ca^{2+}V_{O^{2-}}$ configuration is taken into account, Z' becomes equal to 8, and the conductivity maximum is expected at $x = 1/8 = 0.125$, which is almost twice the observed oxygen vacancy concentration at the maximum. This means that the second and the higher order nearest neighbor $Ca^{2+}V_{O^{2-}}$ configurations also contribute to the effective anion site coordination number of Ca^{2+} , Z' , with a contribution that is equal to that from the first nearest neighbor $Ca^{2+}V_{O^{2-}}$ configuration ($Z' = 8$). This fact seems to be quite reasonable in the light of the rather long-range character of electrostatic interaction between charged defects $Ca^{2+}V_{O^{2-}}$ (18). We might regard the first nearest neighbor Ca^{2+} and $V_{O^{2-}}$ configuration as the ground state of the $(Ca^{2+}V_{O^{2-}})^{\times}$ defect complex, and the second (and the higher order) nearest neighbor $Ca^{2+}V_{O^{2-}}$ configuration as the first excited state (and the higher order excited states) of the $(Ca^{2+}V_{O^{2-}})^{\times}$ defect complex.

But actually the greater the distance between Ca^{2+} and $V_{O^{2-}}$, the more the electrostatic interaction between them would be increasingly screened and weakened. Consequently we include here only the first nearest neighbor and the second nearest neighbor $Ca^{2+}V_{O^{2-}}$ configurations, assuming further that Ca^{2+} coordination number to each 24-second nearest neighbor anion sites is $\sim 1/3$. At this level of approximation, the total effective coordination number of Ca^{2+} to anion sites Z' becomes equal to $(8 \times 1) + (24 \times 1/3) = 16$, which yields the conductivity maximum at $x = 0.0625$ in accordance with experimental observations.

When the CaO content becomes 25 m/o, i.e., $x = 0.125$, the effective anion site coordination number of Ca^{2+} becomes 2, i.e., $Z' \cdot 2x/2 = 2$. This situation is shown in Fig. 2a. Figure 2a shows the unit cell of $Ca_{0.25}Zr_{0.75}O_{1.75}V_{0.125}$ ($x = 0.125$). The unit cell of the fluorite structure contains 4 cations and 8 anions. So at the composition $2x = 1/4$, one out of four cations is Ca^{2+} . In Fig. 3 these Ca^{2+} are situated at the eight corner cation sites of the unit cell. The remaining three cations are Zr^{4+} , which are situated at the face center position of six face planes. One out of 8 anions in the unit cell is $V_{O^{2-}}$ ($x = 1/8$). As is apparent from this figure, 1/4 of the four (= 1) first nearest neighbor cations around $V_{O^{2-}}$ is Ca^{2+} , which yields onefold Ca^{2+} coordination to $V_{O^{2-}}$, and 1/4 of the twelve (= 3) second nearest neighbor cations around $V_{O^{2-}}$ are Ca^{2+} ,

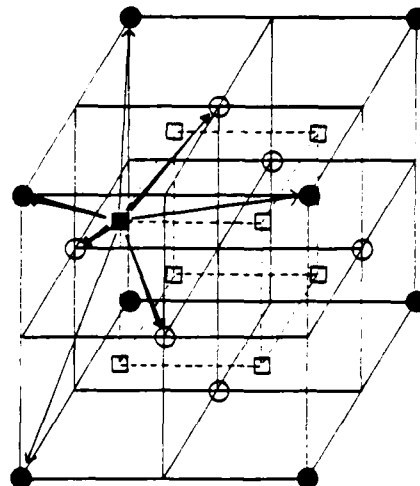


Fig. 2a. Unit cell of the fluorite lattice of $(CaO)_{0.25}(ZrO_2)_{0.75}$ ($2x = 1/4$, $x = 0.125$).

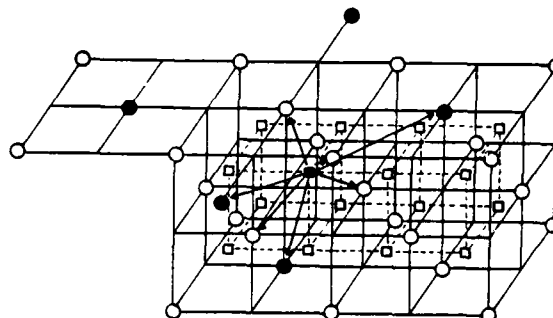


Fig. 2b. $Ca^{2+}V_{O^{2-}}$ configuration in $(CaO)_{0.125}(ZrO_2)_{0.875}$ ($2x = 1/8$, $x = 0.0625$). \bullet Ca^{2+} , \circ Zr^{4+} , \square O^{2-} , \blacksquare $V_{O^{2-}}$, \rightarrow 4 first nearest neighbor cations around $V_{O^{2-}}$, \rightarrow 3 (out of 12) second nearest neighbor Ca^{2+} around $V_{O^{2-}}$.

which yields another onefold coordination to $V_{O^{2-}}$. So, at this composition every $V_{O^{2-}}$ (and anion site) is on an average twofold Ca^{2+} coordinated and every $V_{O^{2-}}$ jump occurs inside effectively twofold associated $(Ca^{2+}V_{O^{2-}})^{\times}$ defect complexes. Similarly, Fig. 2b shows the $Ca^{2+}V_{O^{2-}}$ configuration in $Ca_{0.125}Zr_{0.875}O_{1.875}V_{0.125}$ ($x = 0.0625$) where every two unit cells contain one Ca^{2+} ($2x = 1/8$) and one $V_{O^{2-}}$ ($x = 1/16$). In Fig. 2b, Ca^{2+} are situated at face centered positions of the top plane or bottom plane in an alternative array. Every $V_{O^{2-}}$ (and anion site) is just onefold coordinated by Ca^{2+} , either by one first nearest neighbor Ca^{2+} ($= 1$) or by three second nearest neighbor Ca^{2+} ($1/3 \times 3 = 1$). So at this composition every $V_{O^{2-}}$ jump occurs inside effectively onefold associated $(Ca^{2+}V_{O^{2-}})^{\times}$ defect complexes.

Note that the stabilized cubic fluorite phase appears just when onefold associated $(Ca^{2+}V_{O^{2-}})^{\times}$ defect complexes extend throughout the anion sublattice, giving rise to a conductivity maximum ($x = 0.0625$); and disappears with the disappearance of this defect complex ($x = 0.125$). In these defect concentration ranges, conventional defect equilibria treatments such as Eq. [1] are not applicable, for there exist no more free dissociated anion sites on which $V_{O^{2-}}$ can reside.

Description of the Theoretical Model

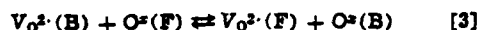
Let us designate at a given composition x , the relatively free state, and the relatively bound state of the

anion sublattice for V_O^{2+} as F and B, respectively. In the case of CSZ within the vacancy concentration range $0.0625 \leq x \leq 0.125$ over which the cubic fluorite phase extends, we can assume that the F-state and the B-state correspond to the 1-fold Ca^{2+} coordinated and 2-fold Ca^{2+} coordinated anion sublattice, respectively. This follows because the Ca^{2+} -average coordination number to the anion sublattice is $1 \leq \frac{Z' \cdot 2x}{2}$

$= 16x \leq 2$. For each concentration of F-state and B-state, the site fractions N_F and N_B will be given by the following equation

$$\begin{aligned} 1 \times N_\text{F} + 2 \times N_\text{B} &= Z' \cdot 2x/2 = 16x, & N_\text{F} + N_\text{B} &= 1, \\ N_\text{F} &= 2 - 16x, & N_\text{B} &= 16x - 1 \\ 0.0625 &\leq x \leq 0.125 \end{aligned} \quad [2]$$

Equation [2] neglects the statistical fluctuations of the system. The distribution of oxygen vacancies V_O^{2+} and oxide ions O^{2-} between these states is assumed to be given by the following quasi-chemical equilibria



Applying the mass action law to Eq. [3] yields

$$\begin{aligned} K &= \exp\left(-\frac{\Delta G^\circ}{RT}\right) = \exp\left(\frac{\Delta S^\circ}{R}\right) \cdot \exp\left(-\frac{\Delta H^\circ}{RT}\right) \\ &= \frac{[\text{V}_\text{O}^{2+}(\text{F})][\text{O}^{2-}(\text{B})]}{[\text{V}_\text{O}^{2+}(\text{B})][\text{O}^{2-}(\text{F})]} \end{aligned} \quad [4]$$

where K , ΔG° , ΔH° , and ΔS° denote the equilibrium constant, standard Gibbs free energy change, standard enthalpy change, and standard entropy change for Eq. [3], respectively, and $[]$ designates the concentration of each chemical species in site fractions.

From the site and mass conservation, the following equations hold

$$\begin{aligned} [\text{V}_\text{O}^{2+}(\text{total})] &= [\text{V}_\text{O}^{2+}(\text{F})] + [\text{V}_\text{O}^{2+}(\text{B})] = x \\ N_\text{F} + N_\text{B} &= 1 \\ [\text{V}_\text{O}^{2+}(\text{F})] + [\text{O}^{2-}(\text{F})] &= N_\text{F} \\ [\text{V}_\text{O}^{2+}(\text{B})] + [\text{O}^{2-}(\text{B})] &= N_\text{B} \end{aligned} \quad [5]$$

Rearranging Eq. [5] yields

$$\begin{aligned} [\text{V}_\text{O}^{2+}(\text{B})] &= x - [\text{V}_\text{O}^{2+}(\text{F})] \\ [\text{O}^{2-}(\text{F})] &= N_\text{F} - [\text{V}_\text{O}^{2+}(\text{F})] \\ [\text{O}^{2-}(\text{B})] &= 1 - N_\text{F} - x + [\text{V}_\text{O}^{2+}(\text{F})] \end{aligned} \quad [6]$$

Inserting Eq. [6] into [4], the following quadratic equation for $[\text{V}_\text{O}^{2+}(\text{F})]$ is obtained

$$\begin{aligned} (1-K)[\text{V}_\text{O}^{2+}(\text{F})]^2 + \{K(x+N_\text{F}) \\ + (1-N_\text{F}-x)\}[\text{V}_\text{O}^{2+}(\text{F})] - K \cdot N_\text{F} \cdot x = 0 \end{aligned} \quad [7]$$

Solving Eq. [7] for $[\text{V}_\text{O}^{2+}(\text{F})]$ (> 0) yields

$$[\text{V}_\text{O}^{2+}(\text{F})] = \frac{-\{K(x+N_\text{F}) + (1-N_\text{F}-x)\} + \sqrt{\{K(x+N_\text{F}) + (1-N_\text{F}-x)\}^2 + 4xK(1-K)N_\text{F}}}{2(1-K)} \quad [8]$$

Then, from Eq. [8] and [6], all the concentrations of each chemical species can be obtained given K and x .

The total ionic conductivity of the system σ_total will be given by the sums of partial ionic conductivity $\sigma_{i,j}$ ($i, j = \text{F, B}$)

$$\sigma_\text{total} = \sum_{i,j=\text{F,B}} \sigma_{i,j} = \sum_{i,j=1,2} \sigma_{i,j} \quad [9]$$

For simplicity, the indexes F and B were designated by 1 and 2 respectively, where $\sigma_{1,1}$ and $\sigma_{2,2}$ designate the partial ionic conductivity due to V_O^{2+} transport through

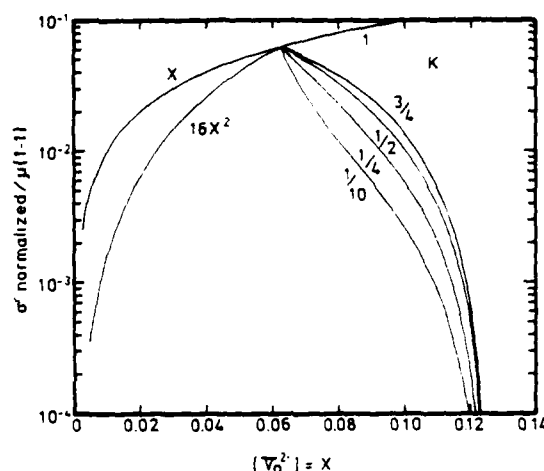


Fig. 3. Schematic variation of σ with oxygen vacancy concentration x when V_O^{2+} transport only through Ca^{2+} -1-fold coordinated anion sublattice is assumed. Numbers beside each curve at $0.0625 \leq x \leq 0.125$ designate K values of Eq. [16].

the channels of the 1-fold Ca^{2+} coordinated and 2-fold Ca^{2+} coordinated anion sublattice, respectively, and $\sigma_{1,2}$ and $\sigma_{2,1}$ designate those due to V_O^{2+} transport from 1- to 2- (or reverse) fold Ca^{2+} -coordinated anion sublattice.

Each partial ionic conductivity will be given by the following expression utilizing the usual form for hopping ionic conduction

$$\begin{aligned} \sigma_{i,j} &= \frac{\sigma_{i,j}}{N \cdot Z \cdot e} \\ &= [\text{V}_\text{O}^{2+}(\text{i})] \cdot \frac{N_j}{N_1 + N_j} \cdot \left(1 - \frac{[\text{V}_\text{O}^{2+}(\text{j})]}{N_j}\right) \cdot \mu_{(i,j)} \\ &= \frac{[\text{V}_\text{O}^{2+}(\text{i})][\text{O}^{2-}(\text{j})]}{N_1 + N_j} \cdot \mu_{(i,j)} \end{aligned} \quad [10]$$

where $\mu_{(i,j)}$ denotes the mobility of V_O^{2+} for the i - j jump process. Each partial ionic conductivity $\sigma_{i,j}$ is normalized by the numerical factor, $(N \cdot Z \cdot e)^{-1}$ from the actual ionic conductivity $\sigma_{i,j}$. In this expression N is numbers of anion sites per unit volume (cm^3), Z is valence number of V_O^{2+} , and e is the electronic charge.

From dynamic equilibria between 1- and 2-states

$$\sigma'_{1,2} = \sigma'_{2,1} \quad [11]$$

Combination of Eq. [4], [10], and [11] yields

$$K = \frac{\mu_{(2,1)}}{\mu_{(1,2)}} = \exp\left(-\frac{\Delta G^\circ}{RT}\right) \quad [12]$$

Equation [12] is the well-known relationship for chemical equilibria resulting from opposing elementary reaction processes.

Inserting Eq. [10] into Eq. [9], the final expression for the normalized total ionic conductivity of the system is obtained

$$\begin{aligned} \sigma'_\text{total} &= \frac{\sigma_\text{total}}{N \cdot Z \cdot e} = \sigma'_{1,1} + \sigma'_{2,2} + 2\sigma'_{2,1} \\ &= [\text{V}_\text{O}^{2+}(\text{1})][\text{O}^{2-}(\text{1})]\mu_{(1,1)} + [\text{V}_\text{O}^{2+}(\text{2})][\text{O}^{2-}(\text{2})]\mu_{(2,2)} \\ &\quad + 2[\text{V}_\text{O}^{2+}(\text{2})][\text{O}^{2-}(\text{1})]\mu_{(2,1)} \quad (N_1 + N_2 = 1) \end{aligned} \quad [13]$$

where $[V_O^{2-}(i)]$ and $[O^{2-}(i)]$ ($i = 1, 2$) are given by Eq. [6] and [8] for a given K and x .

Basic Character of Theoretical Model

We will first examine the theoretical model in more qualitative but illustrative manner. For this purpose, for mathematical simplicity, we will adopt the following approximation in this section: $[V_O^{2-}(i)] \ll [O^{2-}(i)] \approx N_i$ ($i = F, B$), (which corresponds to neglecting the $(1-x)$ term in the conventional $\sigma \propto x(1-x)$ form by assuming $(1-x) \sim 1$). At this level of approximation, Eq. [3] can be easily solved to give

$$[V_O^{2-}(F)] = \frac{x \cdot N_F \cdot \exp(-\Delta G^*/RT)}{N_B + N_F \cdot \exp(-\Delta G^*/RT)} = \frac{x \cdot N_F \cdot K}{N_B + N_F \cdot K}$$

$$[V_O^{2-}(B)] = x - [V_O^{2-}(F)] = \frac{x \cdot N_B}{N_B + N_F \cdot \exp(-\Delta G^*/RT)} = \frac{x \cdot N_B}{N_B + N_F \cdot K} \quad [8']$$

Using Eq. [2] for N_F and N_B , and also Eq. [13] for $\sigma_{\text{normalized}}$ the following expression for $\sigma_{\text{normalized}}$ is obtained, valid for $0.0625 \leq x \leq 0.125$

$$\sigma_{\text{normalized}} = \frac{\sigma_{\text{total}}}{N \cdot Z \cdot e} = \frac{x}{(16x-1) + (2-16x) \cdot K} \times \{ (2-16x)^2 \cdot K \cdot \mu_{(1-1)} + 2(2-16x)(16x-1) \cdot \mu_{(2-1)} + (16x-1)^2 \mu_{(2-2)} \} \quad [14]$$

Following the same procedure, for the composition range $0 \leq x \leq 0.0625$

$$N_F = N_0 = (1-16x): (\text{Ca}^{2+}\text{-0-fold state})$$

$$N_B = N_1 = 16x: (\text{Ca}^{2+}\text{-1-fold state})$$

and

$$\sigma_{\text{normalized}} = \frac{x}{16x + (1-16x) \cdot K'} \times \{ (1-16x)^2 \cdot K' \cdot \mu_{(0-0)} + 2 \cdot (1-16x) \cdot 16x \cdot \mu_{(1-0)} + (16x)^2 \cdot \mu_{(1-1)} \} \quad [15]$$

where $K' = \exp(-\Delta G^{**}/RT)$ and ΔG^{**} designates the Gibbs free energy difference between Ca^{2+} -0-fold and 1-fold states.

When $\Delta G^{**} = \Delta G^* = 0$ ($K' = K = 1$), all the sites become energetically equivalent, so all the $\mu_{(i,j)}$ become equal and $\sigma_{\text{normalized}} \propto x$ from Eq. [14] and [15].

Another interesting limiting case is the one in which ionic conduction occurs exclusively inside the channel of the Ca^{2+} -1-fold coordinated anion sublattice, (i.e., $K' \ll 1$, $\mu_{(1-1)} \gg \mu_{(0-0)}$, $\mu_{(1-0)}$, $K < 1$, $\mu_{(1-1)} \gg \mu_{(2-2)}$, $\mu_{(2-1)}$). In this case from Eq. [14] and [15]

$$\sigma_{\text{normalized}} = x \cdot 16x \cdot \mu_{(1-1)}; \quad 0 \leq x \leq 0.0625$$

$$= \frac{x(2-16x)^2 \cdot \mu_{(1-1)} \cdot K}{(16x-1) + (2-16x) \cdot K} \quad 0.0625 \leq x \leq 0.125 \quad [16]$$

Figure 3 shows $\sigma_{\text{normalized}}/\mu_{(1-1)}$ vs. x curves using $K = \exp(-\Delta G^*/RT)$ as parameter. Included also is the usual curve, $\sigma \propto x$. It is apparent from this figure that if ionic conduction proceeds only via Ca^{2+} -1-fold associated ($\text{Ca}^{2+}\text{-V}_O^{2-}$) defect complexes, there appears a rather sharp conductivity maximum at $x = 0.0625$, and then σ decreases more rapidly, the smaller the value of K .

These features are qualitatively in fair agreement with experimental observations as shown in Fig. 1.

From Eq. [16] the maximum conductivity σ_{max} at $x = 0.0625$ is given by

$$\sigma_{\text{normalized(max)}} = \sigma_{1-1}(x = 0.0625) = 0.0625 \mu_{(1-1)} \quad [17]$$

However, in this approximation, according to Eq. [16] ionic conductivity becomes equal to zero at $x = 0.125$ where the Ca^{2+} -1-fold coordinated anion sublattice disappears. At this composition, only the Ca^{2+} -2-fold coordinated anion sublattice exists (see Fig. 2a), so from Eq. [14] we obtain

$$\sigma_{\text{normalized}}(x = 0.125) = \sigma_{2-2}(x = 0.125) = 0.125 \cdot \mu_{(2-2)} \quad [18]$$

Equations [17] and [18] indicate that from the conductivity data at $x = 0.0625$ and 0.125 , we can obtain the mobility $\mu_{(1-1)}$ and $\mu_{(2-2)}$ inside the separate channels. Using these values of $\mu_{(1-1)}$, $\mu_{(2-2)}$, we can draw the theoretical $\log \sigma$ vs. x curves over the whole range of $0.0625 \leq x \leq 0.125$, choosing appropriate values of K and $\mu_{(2-1)}$.

Numerical Evaluation of the Theoretical Model

In order to obtain mobilities $\mu_{(1-1)}$ and $\mu_{(2-2)}$, approximate values of $\sigma_{\text{total(max)}} = \sigma_{1-1}(x = 0.0625)$, and $\sigma_{\text{total}}(x = 0.125) = \sigma_{2-2}(x = 0.125)$ were read from experimental $\log \sigma$ vs. x plots shown in Fig. 1. For $x = 0.125$ which is well beyond the cubic fluorite phase so that experimental points for σ_{total} are not available, extrapolations from the data points around $x \sim 0.100$ composition were made. Moreover, the values of σ_{max} at $x = 0.0625$ and σ_{total} at $x = 0.125$, were also adjusted to get the best fit between theoretical and experimental curves in the subsequent calculations. At a given pair of such σ 's, $\mu_{(1-1)}$ and $\mu_{(2-2)}$ were calculated from Eq. [17] and [18]

$$\sigma_{\text{max}} = \sigma_{1-1}(x = 0.0625) = x(1-x) \cdot \mu_{(1-1)} = \frac{15}{16^2} \cdot \mu_{(1-1)} \quad [17']$$

$$\sigma_{\text{total}}(x = 0.125) = \sigma_{2-2}(x = 0.125) = x(1-x) \cdot \mu_{(2-2)} = \frac{7}{8^2} \cdot \mu_{(2-2)} \quad [18']$$

Using these values of $\mu_{(1-1)}$ and $\mu_{(2-2)}$, and assuming approximate values of K and $\mu_{(2-1)}$, the theoretical $\log \sigma$ vs. x curves were constructed at each temperature in intervals of $\Delta x = 0.005$ for $0.0625 \leq x \leq 0.125$ until the best fit to the experimental curves was obtained.

At $T = 600^\circ$ and 800°C , the best fits are already obtained without introducing σ_{2-1} terms, i.e., assuming

$\mu_{(2-1)} \sim 0$. At higher temperatures $T = 1000^\circ$, 1200° , and 1400°C , the relative contribution from the partial ionic conductivity σ_{2-1} becomes appreciable, and to obtain the best fit these contributions cannot be neglected.

Results and Discussion

The best fit theoretical curves obtained using the rigorous formula for σ_{total} (Eq. [13]) and for concentrations of the respective chemical species as given by Eq. [6] and [8] are shown in Fig. 1 as solid lines at each temperature within the composition range $0.0625 \leq x \leq 0.125$. Numbers of characteristic parameters used to construct these curves are tabulated in Tables I and II. Also included is the theoretical curve for σ_{total} for $0 \leq x \leq 0.0625$ at 1000°C when it is assumed that only σ_{1-1} contributes to the ionic conductivity: i.e.

$$\sigma_{\text{normalized}} = \frac{\sigma_{1-1}}{N \cdot Z \cdot e} = x(16x-x) \cdot \mu_{(1-1)} = x \cdot 15x \cdot \mu_{(1-1)}, \quad 0 \leq x \leq 0.0625 \quad [13']$$

Agreement between the theoretical curves and the experimental ones is quite satisfactory over the entire

Table I. K , σ_{\max} ($x = 0.0625$), and σ ($x = 0.125$) used to construct the theoretical curves in Fig. 1

T (°C)	$\sigma_{\max} = \sigma_{1-1}$ ($x = 0.0625$) ($\Omega \cdot \text{cm}$) ⁻¹	$\sigma_{2-2} = \sigma$ ($x = 0.125$) ($\Omega \cdot \text{cm}$) ⁻¹	K
600	7.341×10^{-4}	5.203×10^{-4}	0.060
800	1.185×10^{-3}	4.0×10^{-4}	0.12
1000	7.013×10^{-3}	4.5×10^{-4}	0.20
1200	2.70×10^{-1}	4.2×10^{-4}	0.28
1400	6.40×10^{-1}	2.0×10^{-1}	0.37

Table II. Mobility of oxygen vacancy $V_{O^{2-}}$ ($i-j$) ($i = 1, 2$) through and between Ca^{2+} -1-fold and Ca^{2+} -2-fold coordinated anion sublattice

T (°C)	$\mu_{(1-1)}$ (cm ² /sec V)	$\mu_{(2-2)}$ (cm ² /sec V)	$\mu_{(1-2)}$ (cm ² /sec V)	$\mu_{(2-1)}$ (cm ² /sec V)
600	6.684×10^{-7}	2.507×10^{-6}	—	—
800	1.046×10^{-6}	1.927×10^{-6}	—	—
1000	6.306×10^{-6}	2.166×10^{-6}	6.500×10^{-7}	3.25×10^{-7}
1200	2.428×10^{-5}	2.024×10^{-5}	1.500×10^{-5}	5.357×10^{-6}
1400	5.756×10^{-5}	9.640×10^{-5}	7.500×10^{-5}	2.027×10^{-4}

temperature range: $600^\circ\text{C} \leq T \leq 1400^\circ\text{C}$ and the stability range of the cubic fluorite phase: $0.0625 \leq x \leq 0.10$.

Figure 4 shows Arrhenius plots of $\sigma_{1-1}(x)$ ($i = 1, 2$; $x = 0.0625, 0.125$) and $\sigma_{1-1}(x) \cdot T$ ($i = 1, 2$; $x = 0.0625, 0.125$). From this figure, we can obtain the Arrhenius equations for σ_{1-1} and $\sigma_{1-1} \cdot T$, respectively

$$\sigma_{1-1}(x = 0.0625) = \sigma_{\max} = 1.138 \cdot 10^3$$

$$\exp\left(-\frac{25.022 \text{ kcal/mole}}{RT}\right) (\Omega \cdot \text{cm})^{-1}$$

$$\sigma_{2-2}(x = 0.125) = 2.317 \cdot 10^4$$

$$\cdot \exp\left(-\frac{38.835 \text{ kcal/mole}}{RT}\right) (\Omega \cdot \text{cm})^{-1} \quad [19]$$

and

$$\sigma_{1-1}(x = 0.0625) \cdot T = \sigma_{\max} \cdot T = 4.57 \cdot 10^6$$

$$\cdot \exp\left(-\frac{27.474 \text{ kcal/mole}}{RT}\right) (\Omega \cdot \text{cm})^{-1} \cdot ^\circ\text{K}$$

$$\sigma_{2-2}(x = 0.125) \cdot T = 7.18 \cdot 10^7$$

$$\cdot \exp\left(-\frac{40.936 \text{ kcal/mole}}{RT}\right) (\Omega \cdot \text{cm})^{-1} \cdot ^\circ\text{K} \quad [20]$$

To obtain the actual value of ionic conductivity the number of charge carriers per cubic centimeter is necessary. To this end, the average lattice constant: $a_0 = 5.131 \text{ \AA}$ (1) for the nominal composition $\text{Ca}_{0.15}\text{Zr}_{0.85}\text{O}_{1.85}$ was adopted, neglecting the relatively small variation of a_0 with composition. Then

$$\sigma_{1-1}(x) (i = 1, 2; x = 0.0625, 0.125)$$

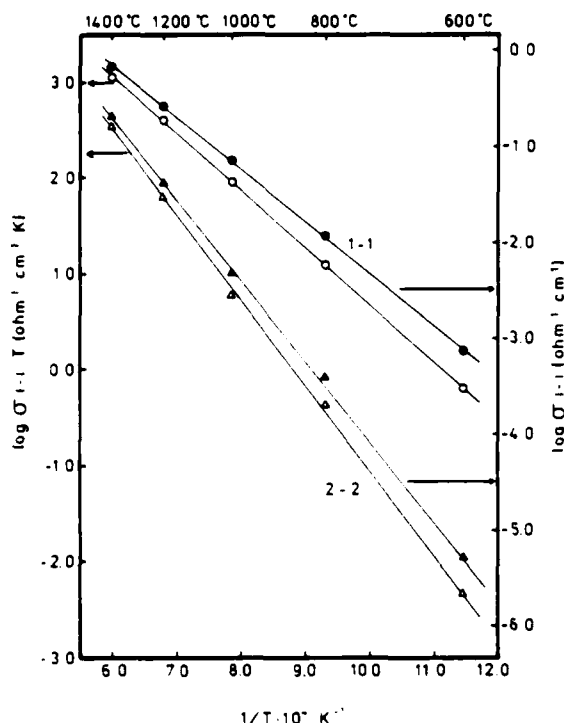
$$= N \cdot Z \cdot e \cdot x(1-x) \cdot \mu_{(1-1)}$$

$$= N \cdot x(1-x) \cdot \frac{Z^2 \cdot e^2 \cdot D_{(1-1)}}{kT} \quad [21]$$

where N is the number of anion sites per cm³ and given $N = 5.922 \times 10^{22}/\text{cm}^3$ using the above a_0 value. In the latter part of Eq. [21] the Nernst-Einstein relation was used

$$\mu_{(1-1)} = \frac{Z \cdot e \cdot D_{(1-1)}}{kT} \quad [22]$$

Combining Eq. [19], [20], and [21] leads to the Arrhenius equations for $\mu_{(1-1)}$ and $D_{(1-1)}$

Fig. 4. $\log \sigma_{1-1}(x)$ and $\log \sigma_{1-1}(x) \cdot T$ ($x = 0.0625, 0.125$, $i = 1, 2$) vs. $1/T$ plots.

$$\mu_{(1-1)} = 1.19 \cdot \exp\left(-\frac{25.022 \text{ kcal/mole}}{RT}\right) \text{ cm}^2 \cdot \text{sec}^{-1} \cdot \text{V}^{-1}$$

$$\mu_{(2-2)} = 1.16 \cdot 10^3 \cdot \exp\left(-\frac{38.835 \text{ kcal/mole}}{RT}\right) \text{ cm}^2 \cdot \text{sec}^{-1} \cdot \text{V}^{-1} \quad [23]$$

$$D_{(1-1)} = 1.77 \cdot 10^{-1} \cdot \exp\left(-\frac{27.474 \text{ kcal/mole}}{RT}\right) \text{ cm}^2 \cdot \text{sec}^{-1}$$

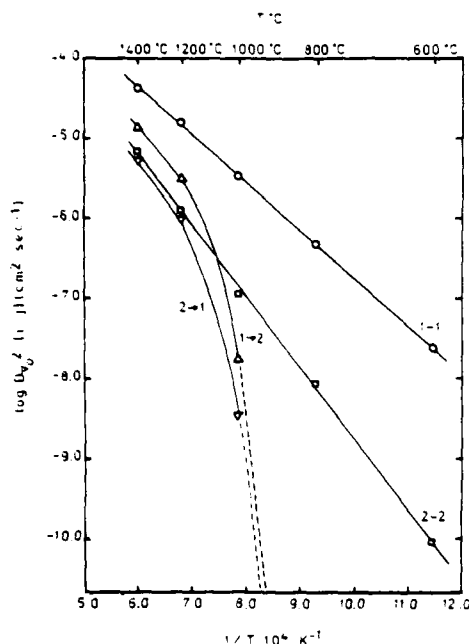
$$D_{(2-2)} = 1.49 \cdot 10^0 \cdot \exp\left(-\frac{40.936 \text{ kcal/mole}}{RT}\right) \text{ cm}^2 \cdot \text{sec}^{-1} \quad [24]$$

Values of $\mu_{(i-j)}$ and $D_{(i-j)}$ are tabulated in Tables II and III, respectively, together with $\mu_{(i-j)}$ ($i \neq j = 1, 2$) and $D_{(i-j)}$, which were also used to derive the theoretical curves. To obtain $\mu_{(1-2)}$ from $\mu_{(2-1)}$ Eq. [12] and K values in Table I were used.

Figure 5 shows Arrhenius plots of the various diffusion coefficients of the oxygen vacancy $D_{(i-j)}$. From this figure it is apparent that $D_{(1-1)} \gg D_{(2-2)} \sim D_{(1-2)}$

Table III. Diffusion coefficients of oxygen vacancy $V_{O^{2-}}$ $D_{(i-j)}$ through and between Ca^{2+} -1-fold and Ca^{2+} -2-fold coordinated anion sublattice

T (°C)	$D_{(1-1)}$ (cm ² /sec)	$D_{(2-2)}$ (cm ² /sec)	$D_{(1-2)}$ (cm ² /sec)	$D_{(2-1)}$ (cm ² /sec)
600	2.514×10^{-8}	9.429×10^{-11}	—	—
800	4.844×10^{-7}	8.910×10^{-9}	—	—
1000	3.459×10^{-6}	1.189×10^{-7}	3.565×10^{-8}	1.783×10^{-8}
1200	1.541×10^{-5}	1.284×10^{-6}	9.521×10^{-7}	3.400×10^{-7}
1400	4.149×10^{-5}	6.946×10^{-6}	3.407×10^{-6}	1.461×10^{-6}

Fig. 5. $\log D_{Vo^{2+}} (i-j)$, $j = 1, 2$ vs. $1/T$ plots

$> D_{(2 \rightarrow 1)}$ as expected. This means that diffusion of Vo^{2+} through the relatively free state (1-1) proceeds much more easily with a lower activation energy and with a higher absolute value than that through the relatively more bound state (2-2).

An interesting feature of $D_{(2 \rightarrow 1)}$ and $D_{(1 \rightarrow 2)}$ is the fact that there exists a rather sharp kink in the Arrhenius plots for $D_{(2 \rightarrow 1)}$ and $D_{(1 \rightarrow 2)}$ around and below 1000°C. Indeed, as was mentioned in the previous section, the theoretical curves at $T = 600^\circ$ and 800° C were constructed without any contribution from $\sigma_{(2 \rightarrow 1)}$, and yet shows good agreement with the experimental ones. At 1000°C, their contributions are still small but at higher temperatures $T = 1200^\circ$ and 1400° C, they become considerable. It seems premature to draw any definite conclusion concerning the origin of this phenomenon. However, it is interesting to note that even in "disordered" samples, it is often reported that there seems to exist a slight hump in the Arrhenius plots of $\log \sigma$ vs. $1/T$ above 1000°C, which becomes more apparent in the samples with higher CaO content (1, 5). Figure 6 shows the $\log K$ vs. $1/T$ plot for the chemical equilibria given by Eq. [3] and tabulated in Table I. A good straight line relationship holds for 600° C $\leq T \leq 1400^\circ$ C. From this figure we obtain for the equilibrium constant K

$$K = \exp \left(\frac{\Delta S^\circ}{R} \right) \cdot \exp \left(- \frac{\Delta H^\circ}{RT} \right) = \exp \left(- \frac{\Delta G^\circ}{RT} \right) \\ = 2.7 \cdot \exp \left(- \frac{6.606 \text{ kcal/mole}}{RT} \right) \quad [4']$$

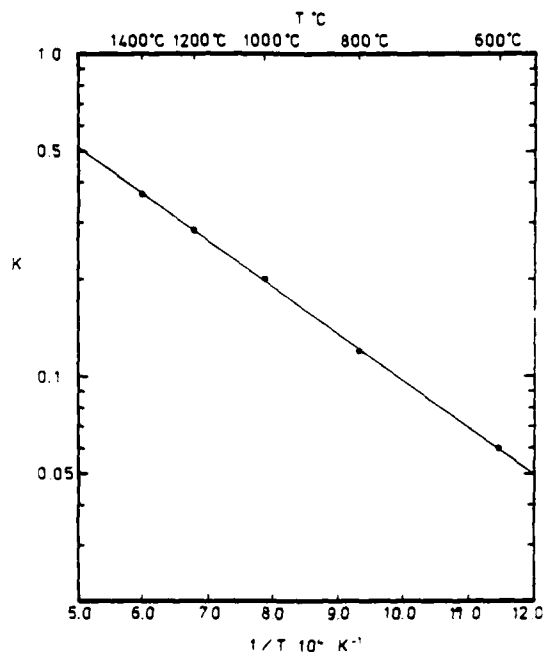
Accordingly

$$\Delta S^\circ = 0.993 \text{ eu} = 1.974 \text{ cal/mole} \cdot \text{K} \sim R$$

$$\Delta H^\circ = 6.606 \text{ kcal/mole}$$

$$\Delta G^\circ = \Delta H^\circ - T\Delta S^\circ = 6.606 \times 10^3 - 1.974 \cdot T \text{ cal/mole} \quad [25]$$

Figure 7 shows the variations of oxygen vacancy concentrations on the Ca^{2+} -1-fold coordinated and

Fig. 6. $\log K$ vs. $1/T$ plot

Ca^{2+} -2-fold coordinated anion sublattices; Vo^{2+} (1) and Vo^{2+} (2), with total oxygen vacancy concentration $[Vo^{2+}]_{\text{total}} = x$ at 600° , 1000° , and 1400° C calculated according to Eq. [6] and [8]. Also included in Fig. 7 are the site fractions of 1- and 2-state; N_1 and N_2 . It is interesting to note that the variations of $[Vo^{2+} \cdot 1]$ and $[Vo^{2+} \cdot 2]$ with x is steepest at $x = 0.0625$ and become more gradual with increasing x . The equiconcentration point $[Vo^{2+} \cdot 1] = [Vo^{2+} \cdot 2]$ shifts to the higher x value position as temperature increases, but remains in the low x region in these temperature ranges.

Experiment shows that the activation energy for ionic conduction increases with increasing x and decreases with increasing temperature at constant x . Both features are accounted for by the present model. These follow because with increasing x , the relative contributions from $\sigma_{1 \rightarrow 2}$ and $\sigma_{2 \rightarrow 2}$ which have activation energies higher than $\sigma_{1 \rightarrow 1}$ increase, and, as shown in Fig. 7 at constant x , the higher the temperature, the higher the relative contribution from $[Vo^{2+} \cdot 1]$ and hence the contribution from $\sigma_{1 \rightarrow 1}$, which has the lower activation energy, increases.

Oxygen diffusion measurements on this system reported so far are those by Kingery et al. (19), Simpson and Carter (20), and Hagel (21). References (19) and (20) report agreement of the measured oxygen diffusion coefficient $D_{O^{18}}$ with that calculated from ionic conductivity assuming an oxygen transport number of 1 and the correlation factor of 0.65 for the fluorite structure. In contrast, Hagel (21) obtained an oxygen diffusion coefficient $D_{O^{18}}$ appreciably lower than that calculated from his own conductivity data. If the ionic conduction and therefore the oxygen diffusion in this system are multimode processes as described by the present model, the penetration profile of O^{18} from the gas phase would not yield a curve characterized by one error function complement. Such experiments are quite difficult to carry out and, depending on the relative contributions of each mode, the result may appear to fit a single error function complement as was shown for the diffusion of sulfur in NiO by Howng and Wagner (22).

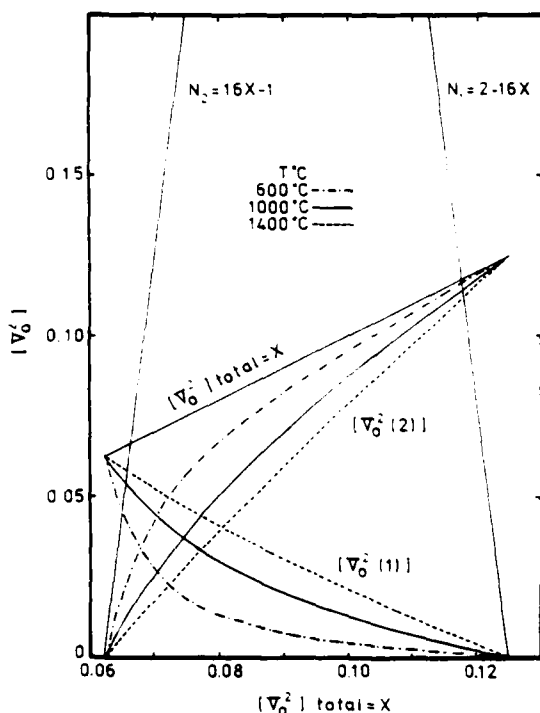


Fig. 7. Oxygen vacancy distribution between Ca^{2+} -1-fold and Ca^{2+} -2-fold coordinated anion sublattice as a function of total oxygen vacancy concentration $[\text{V}_{\text{O}^{2+}}]_{\text{total}} = x$. $T = 600^\circ\text{C}$, 1000°C , 1400°C . $[\text{V}_{\text{O}^{2+}} (1)]$: oxygen vacancy concentration on Ca^{2+} -1-fold coordinated anion sublattice. $[\text{V}_{\text{O}^{2+}} (2)]$: oxygen vacancy concentration on Ca^{2+} -2-fold coordinated anion sublattice. N_1 : site fraction of Ca^{2+} -1-fold coordinated anion sublattice. N_2 : site fraction of Ca^{2+} -2-fold coordinated anion sublattice.

Internal friction measurements on this system conducted by Wachtman and Corwin (23) seem to support the above speculation on the oxygen diffusion coefficient and partially substantiate our proposed theoretical model. Wachtman and Corwin observed the symmetrical peaks associated with $\text{V}_{\text{O}^{2+}}$ motion in the cubic fluorite phase region, but the peaks were too broad to result from a relaxation process with a single relaxation time. They thought that the concentrations of $\text{V}_{\text{O}^{2+}}$ and Ca^{2+} are so high that many complex groupings and/or various arrangements of Ca^{2+} and $\text{V}_{\text{O}^{2+}}$ occur which cause the various types of local $\text{V}_{\text{O}^{2+}}$ jumps and therefore a distribution of relaxation times. Their interpretation is similar to that of Kröger (10) mentioned previously.

As was shown in the foregoing, the proposed theoretical model seems to succeed to some extent in giving a quantitative character to these qualitative interpretations. The basic feature of the theoretical model is that it extends the conventional concept of dopant (impurity)-defect complex or associate for highly defective systems and shows in a straightforward way the occurrence of a maximum of the ionic conductivity and a multimode transport mechanism for these systems. However, in formulating the theoretical model, crude assumption for the effective anion site coordination number of Ca^{2+} to the second nearest neighbor (Ca^{2+} - $\text{V}_{\text{O}^{2+}}$) configuration was made. So far, our knowledge about defect interaction at the second (and the higher order) nearest neighbor configuration is quite lacking. Moreover, the statistical fluctuations of the system were also neglected. (See Eq. [2]). Even in the composition range $0.0625 \leq x \leq 0.125$, there exist also small numbers of Ca^{2+} -0-fold, 3-fold, 4-fold anion sites, which were all neglected. Also, the existence of

nonintegrally Ca^{2+} coordinated sites such as Ca^{2+} -1/3-fold, Ca^{2+} -5/3-fold anion sites were neglected.) These fluctuations would be dependent on the Ca^{2+} distribution and should be important in dealing with the order-disorder transition in this system.

Summary

A quantitative theoretical model to explain the variations of ionic conductivity of calcia-stabilized zirconia with oxygen vacancy concentration and temperature has been presented. The theory extends the conventional concept of the impurity (dopant)-defect complex or associate for highly defective systems and shows that ionic conduction in this system proceeds by a multimode mechanism: Eq. [13]. The theory predicts the occurrence of a rather sharp maximum of ionic conductivity at oxygen vacancy concentration $x \sim 0.0625$ (12.5 m/o CaO), at which the entire anion sublattice is just covered by onefold associated (Ca^{2+} - $\text{V}_{\text{O}^{2+}}$) complexes, in accordance with experimental observations.

Values of characteristic parameters such as the diffusion coefficients and mobilities of oxygen vacancies $\text{V}_{\text{O}^{2+}}$ through and between 1-fold and 2-fold Ca^{2+} coordinated anion sublattice; $D_{(1-1)}$, $\mu_{(1-1)}$, and the equilibrium constant K for the distribution of oxide ions and oxygen vacancies between 1-fold and 2-fold Ca^{2+} coordinated anion sublattice were obtained by a curve-fitting procedure of the theoretical expression for ionic conductivity to experimental $\sigma(x, T)$ data reported in the literature. Resultant theoretical curves of isothermal $\log \sigma$ vs. oxygen vacancy concentration x , inside the stability region of the cubic fluorite phase $0.0625 \leq x \leq 0.10$ and $600^\circ\text{C} \leq T^\circ\text{C} \leq 1400^\circ\text{C}$ were shown to reproduce satisfactorily the experimental curves reported by various investigators.

Acknowledgment

This research was sponsored by the United States Army Research Office under Contract DAAG 29-78-G-0032.

Manuscript submitted Dec. 14, 1979; revised manuscript received April 30, 1980. This was Paper 53 presented at the St. Louis, Missouri, Meeting of the Society, May 11-16, 1980.

Any discussion of this paper will appear in a Discussion Section to be published in the June 1981 JOURNAL. All discussions for the June 1981 Discussion Section should be submitted by Feb. 1, 1981.

Publication costs of this article were assisted by Arizona State University.

REFERENCES

1. See comprehensive review by T. H. Etsell and S. N. Flengas on these subjects: i.e., T. H. Etsell and S. N. Flengas, *Chem. Rev.*, **70**, 339 (1970).
2. D. W. Strickler and W. G. Carlson, *J. Am. Ceram. Soc.*, **47**, 122 (1964).
3. T. Y. Tien, *ibid.*, **47**, 430 (1964).
4. J. M. Dixon, L. D. LaGrange, U. Merten, C. F. Miller, and J. T. Porter, *ibid.*, **110**, 276 (1963).
5. T. Y. Tien and E. C. Subbarao, *J. Chem. Phys.*, **39**, 1041 (1963).
6. R. E. W. Casselton, *Phys. Status Solidi A*, **2**, 571 (1970).
7. M. F. Lasker and R. A. Rapp, *Z. Phys. Chem. N.F.*, **49**, 198 (1966).
8. R. N. Blumenthal, F. S. Brugner, and J. E. Garnier, *This Journal*, **120**, 1230 (1973).
9. D. W. Strickler and W. G. Carlson, *J. Am. Ceram. Soc.*, **48**, 286 (1965).
10. F. A. Kröger, *ibid.*, **49**, 215 (1966).
11. M. O'Keefe, in "Chemistry of the Extended Defects in Non-Metallic Solids," L. Eyring and M. O'Keefe, Editors, p. 609, North Holland Publishing Co., Amsterdam (1970).
12. W. W. Barker and O. Knop, *Proc. Br. Ceram. Soc.*, **19**, 15 (1971).
13. A. Hammou, *J. Chim. Phys.*, **72**, 439 (1975).

14. A. B. Lidiard, *Phys. Rev.*, **94**, 29 (1954).
15. H. Schmalzried, *Z. Phys. Chem., N.F.*, **105**, 47 (1977).
16. R. E. Carter and W. L. Roth, in "Electromotive Force Measurements in High Temperature Systems," C. B. Alcock, Editor, p. 125, I.M.M., London (1968).
17. E. C. Subbarao and P. H. Sutter, *J. Phys. Chem. Solids*, **25**, 149 (1964).
18. J. S. Anderson, in "Problems of Nonstoichiometry," A. Rabenau, Editor, p. 1, American Elsevier Publishing Co., New York (1970).
19. W. D. Kingery, J. Pappis, M. E. Doty, and D. C. Hill, *J. Am. Ceram. Soc.*, **42**, 393 (1959).
20. L. A. Simpson and R. E. Carter, *ibid.*, **49**, 139 (1966).
21. W. C. Hagel, *This Journal*, **110**, 63C (1963), quoted in Ref. (20).
22. W. Y. Hwang and J. B. Wagner, Jr., *J. Phys. Chem. Solids*, **39**, 1019 (1978).
23. J. B. Wachtman, Jr. and W. G. Corwin, *J. Res. Natl. Bur. Stand., A69*, 457 (1965).

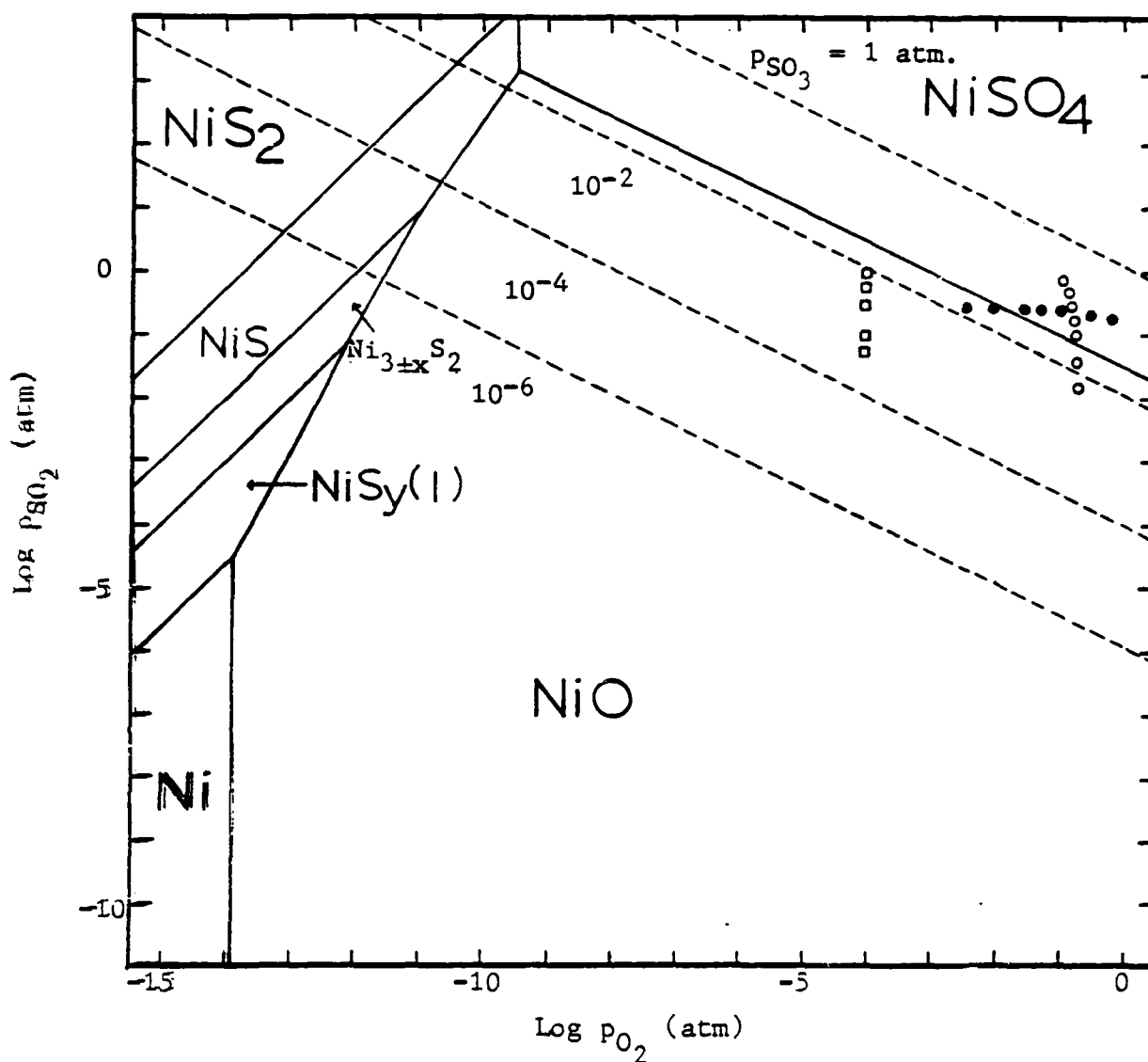
LIST OF ALL PUBLICATIONS

AND TECHNICAL REPORTS:

- A. Nakamura and J.B. Wagner, Jr. "Defect Structure, Ionic Conductivity and Diffusion in Calcia-Stabilized Zirconia," J. Electrochem. Soc. 127 pp. 2324-2333 (1980)

MANUSCRIPTS IN PREPARATION

- A. Nakamura and J.B. Wagner, Jr. " S^{35} and Te^{127m} Impurity Diffusion in 15 m/o CaO - Stabilized Zirconia".
- A. Nakamura and J.B. Wagner Jr. "Defect Structure, Ionic Conductivity and Diffusion in Yittria Stabilized Zirconia and Related Oxide Electrolytes with Fluorite Structure."
- H. Yagi and J.B. Wagner, Jr. "Corrosion of Nickel in SO_2 - O_2 -Ar Gas mixtures at 800°C."



STABILITY DIAGRAM OF Ni-O₂-SO₂ SYSTEM AT 800°C

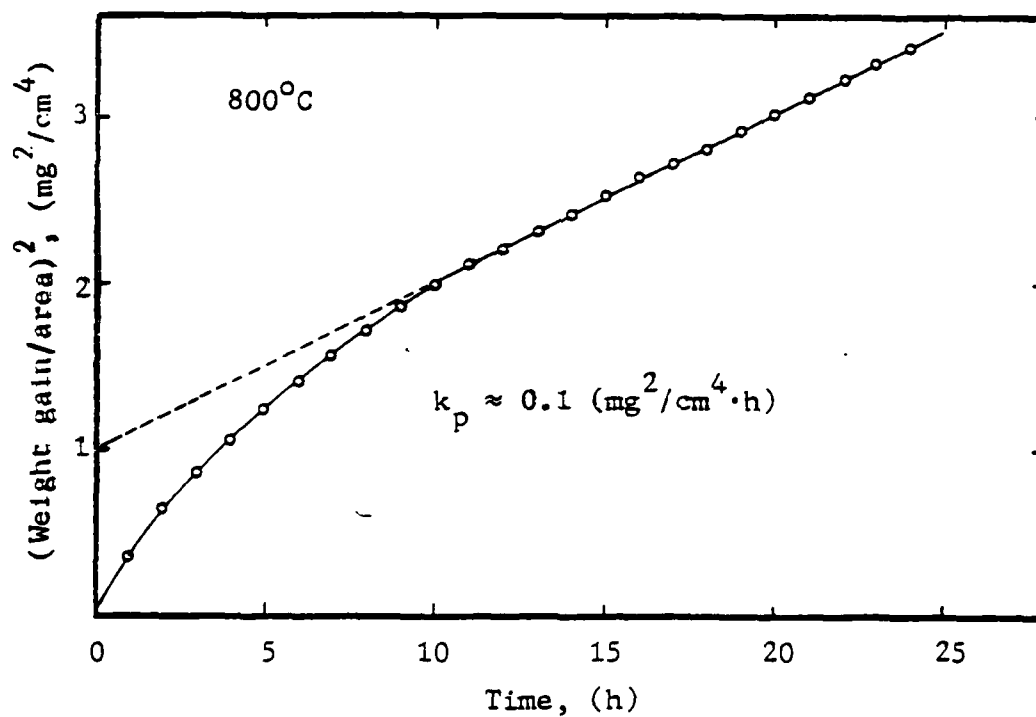
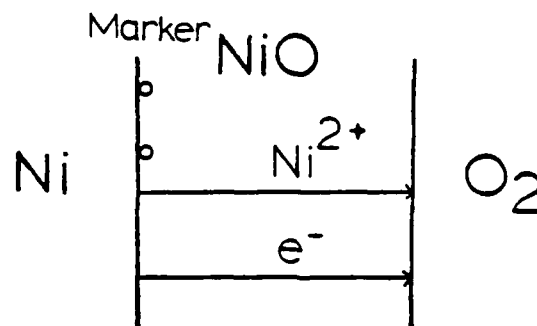
GAS MIXTURES: ○ 20% O₂ + Variable SO₂ + Balance Ar

● 30% SO₂ + Variable O₂ + Balance Ar

□ Variable SO₂ + Balance Ar

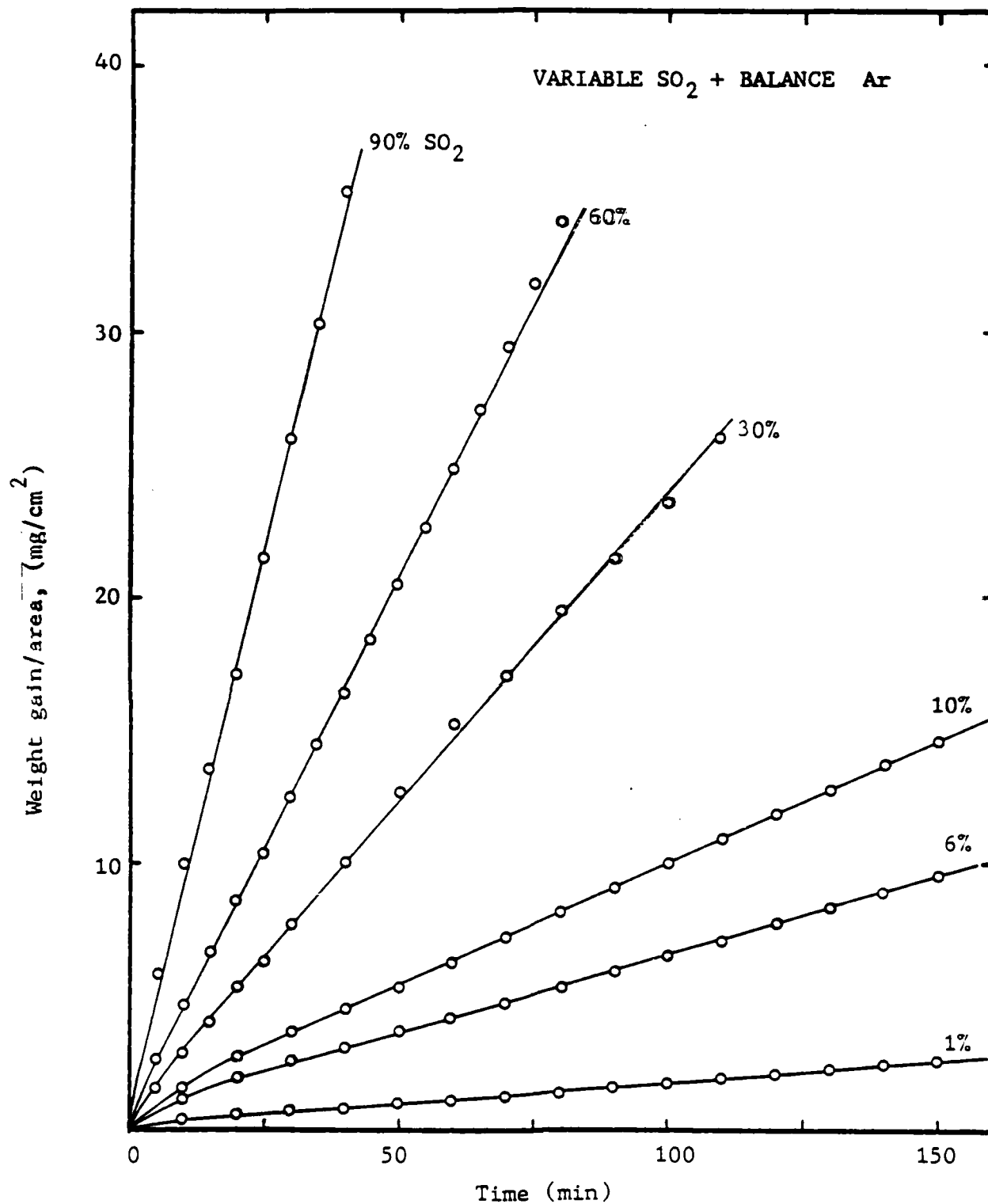
FIGURE 1. Stability diagram of the Ni-O₂-SO₂ system at 800°C.

For the variable SO₂-balance argon gas mixtures, an oxygen partial pressure of $\sim 10^{-5}$ Torr was in the argon.



Parabolic Plot of Oxidation of Nickel
in 0.2 atm O_2 at 800° C

FIGURE 2. (TOP) Schematic diagram of location of P+ marker after oxidation in 0.2 atm O_2 at 800° C. (BOTTOM) The value of k_p is consistent with literature data.



WEIGHT GAIN VS TIME FOR NICKEL AT 800°C

FIGURE 3. Linear corrosion kinetics for nickel in SO_2 -Ar gas mixtures ($P = P_{\text{SO}_2} + P_{\text{Ar}} = 1$ atm total pressure). 800°C .

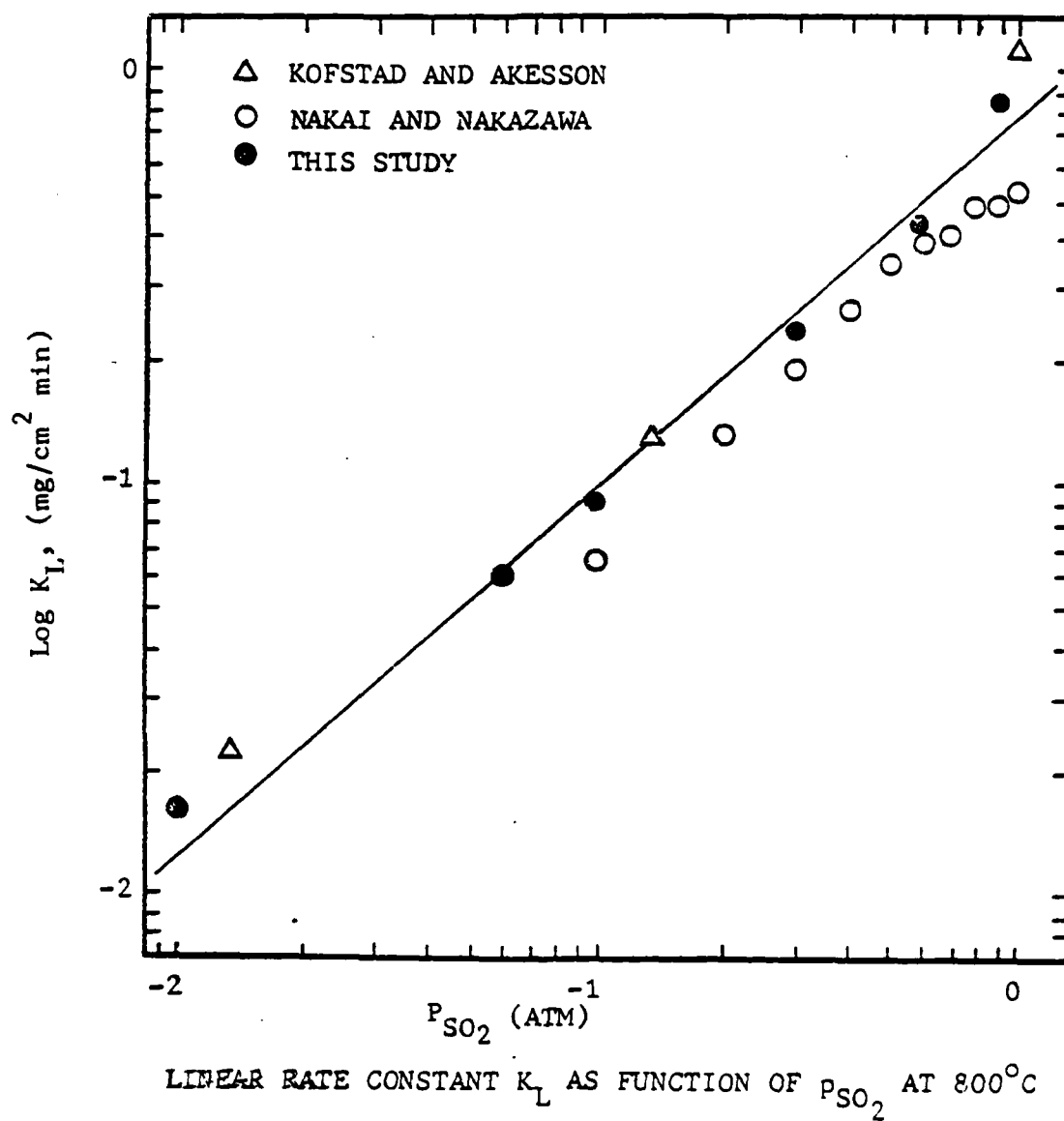
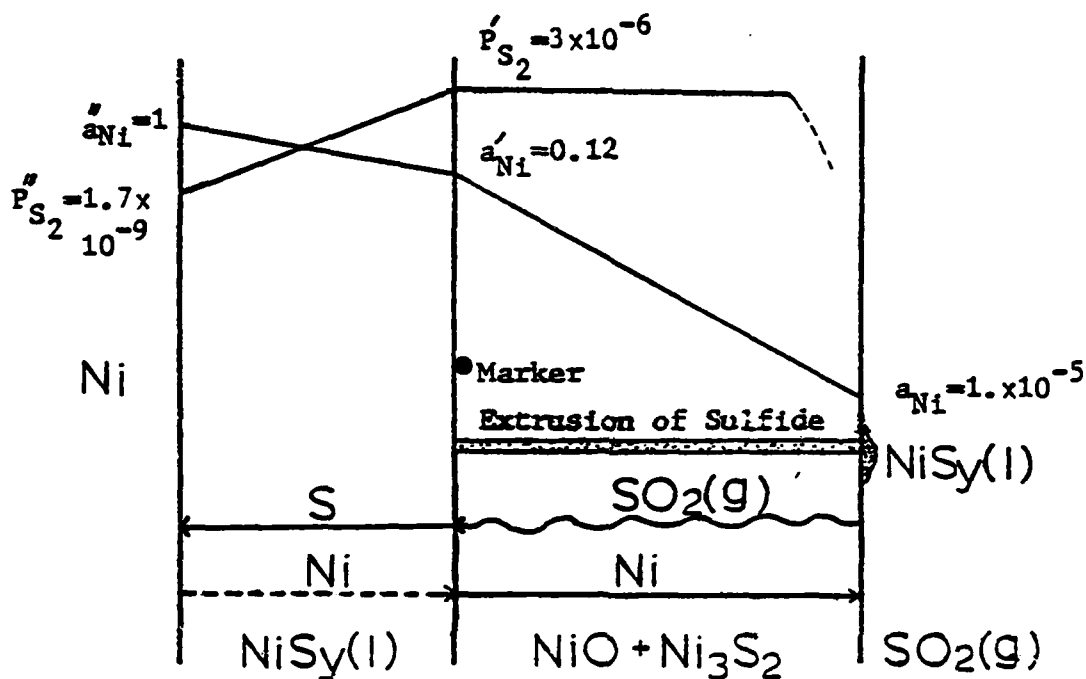
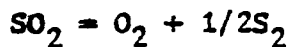


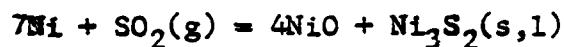
FIGURE 4. Linear rate constant, K_L , for SO_2 -Ar gas mixtures at 800°C .

CORROSION MECHANISM IN PURE SO₂ (2)

REACTION AT SULFIDE/OXIDE Interface;



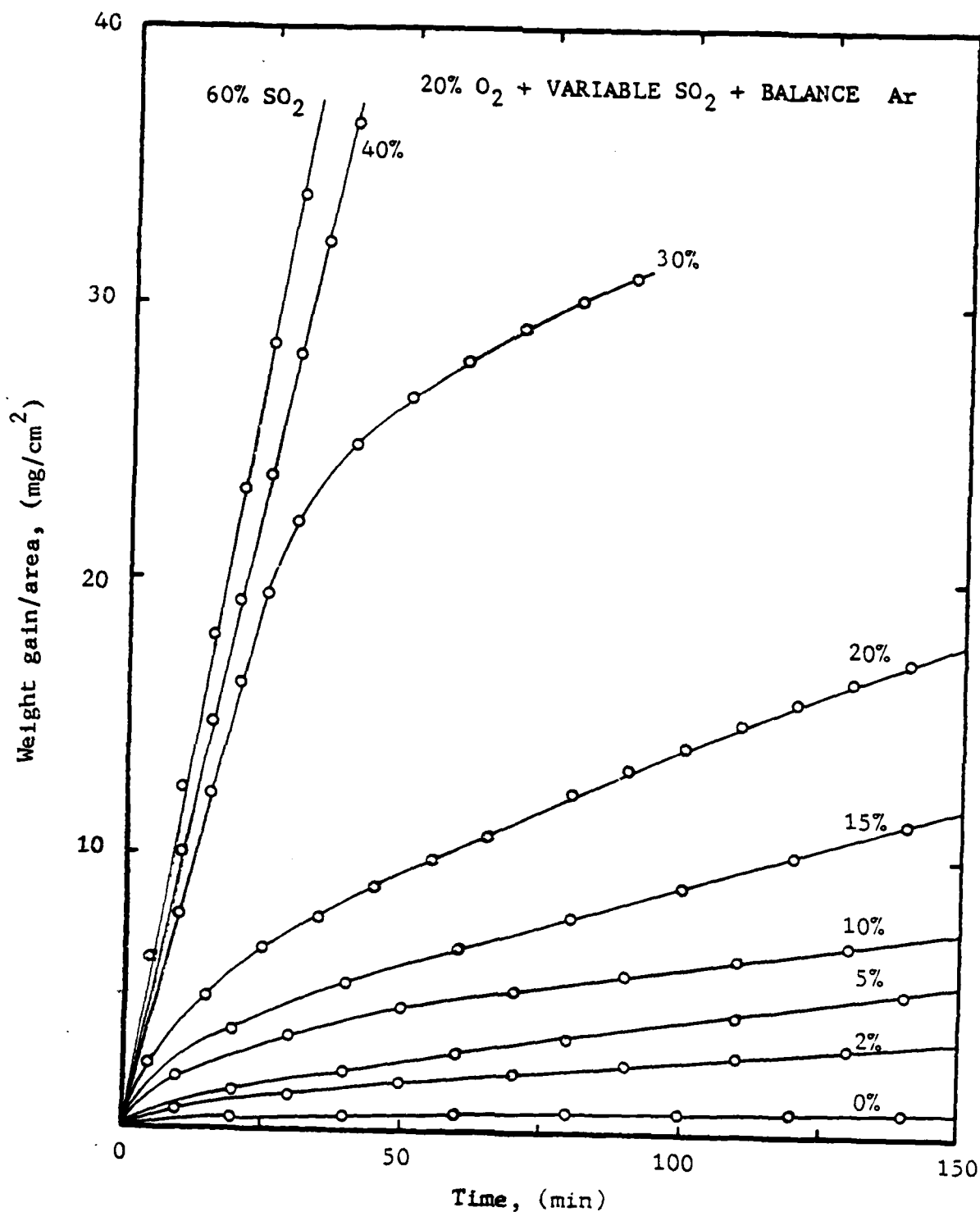
$P'_{\text{SO}_2} \geq 3.0 \times 10^{-5}$ (atm) For Sulfide Formation
When $a_{\text{Ni}} = 1$



$P'_{\text{SO}_2} \geq 0.1$ (atm) When $a_{\text{Ni}} = 0.12$

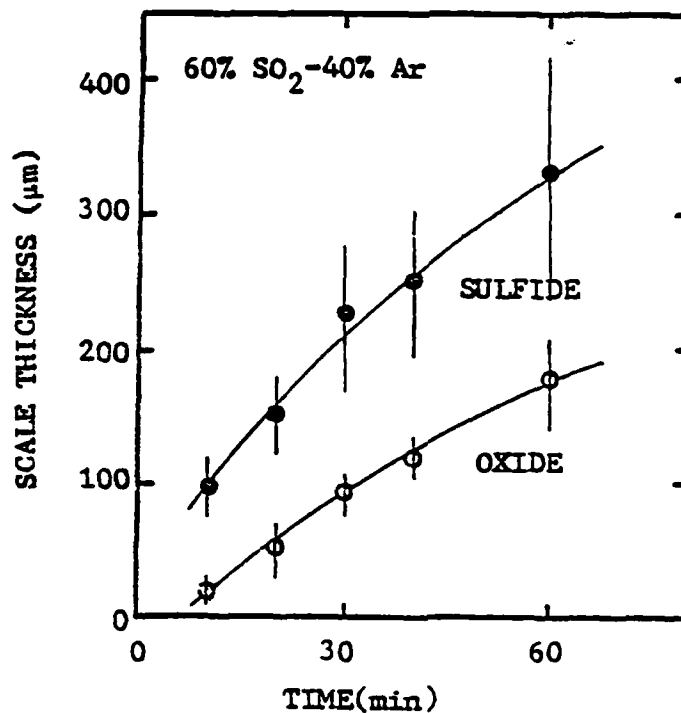
$P'_{\text{SO}_2} \geq 5.3 \times 10^{-5}$ (atm) When $a_{\text{Ni}} = 1.0$

FIGURE 5. Possible mechanism for corrosion of nickel in SO₂-Ar gas mixtures at 800°C. The rate determining step for the observed linear kinetics is the dissociation of SO₂(ads) on the sulfide inner layer.

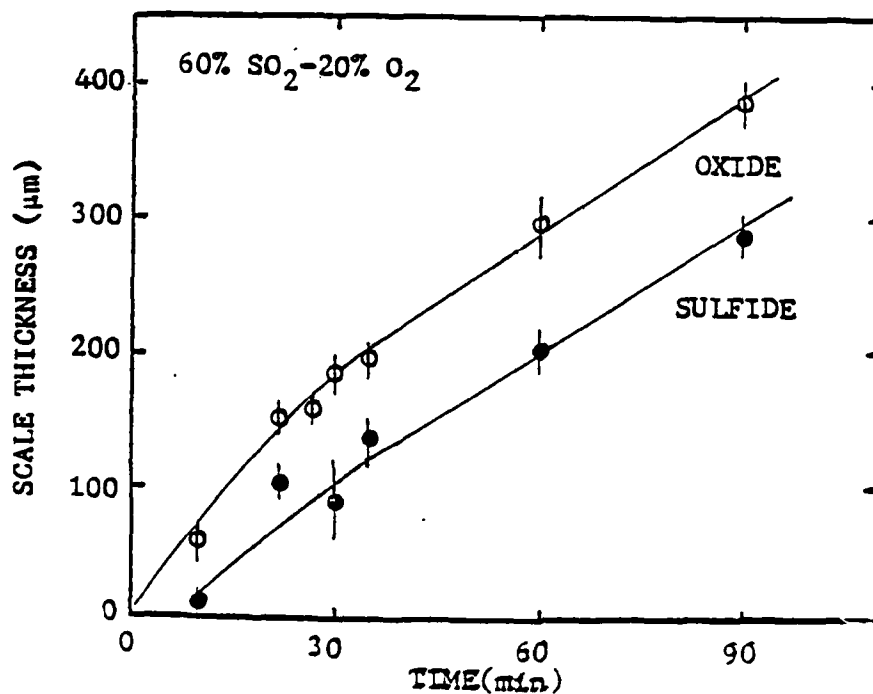


WEIGHT GAIN VS TIME FOR NICKEL AT 800°C

FIGURE 6. Kinetics for 20% O₂-variable SO₂-balance argon at 800°C. Note the two regimes, one $\leq 20\%$ in which the corrosion is protective and one $\geq 30\%$ in which the kinetics are extremely rapid.

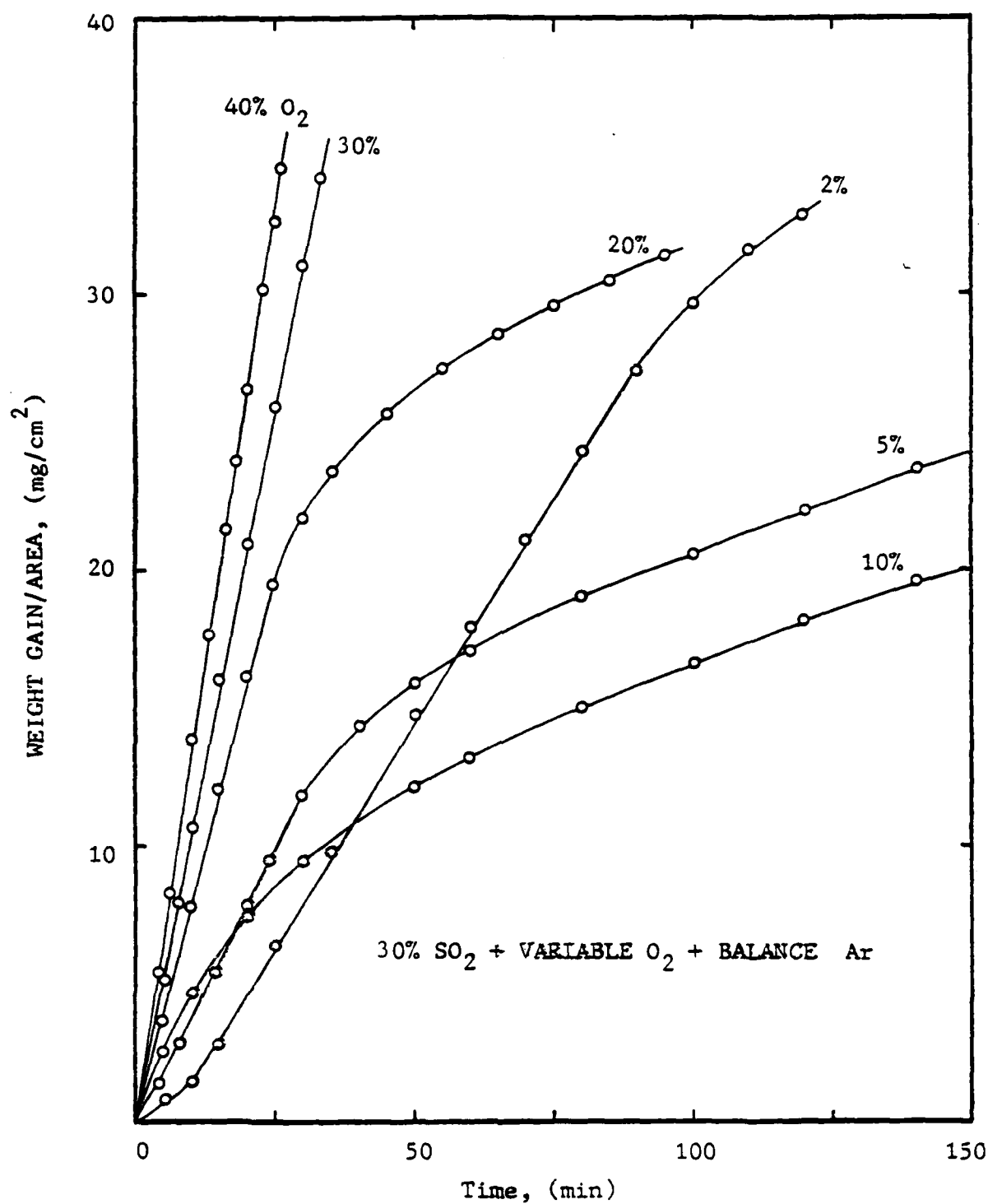


SCALE THICKNESS AS A FUNCTION OF TIME.



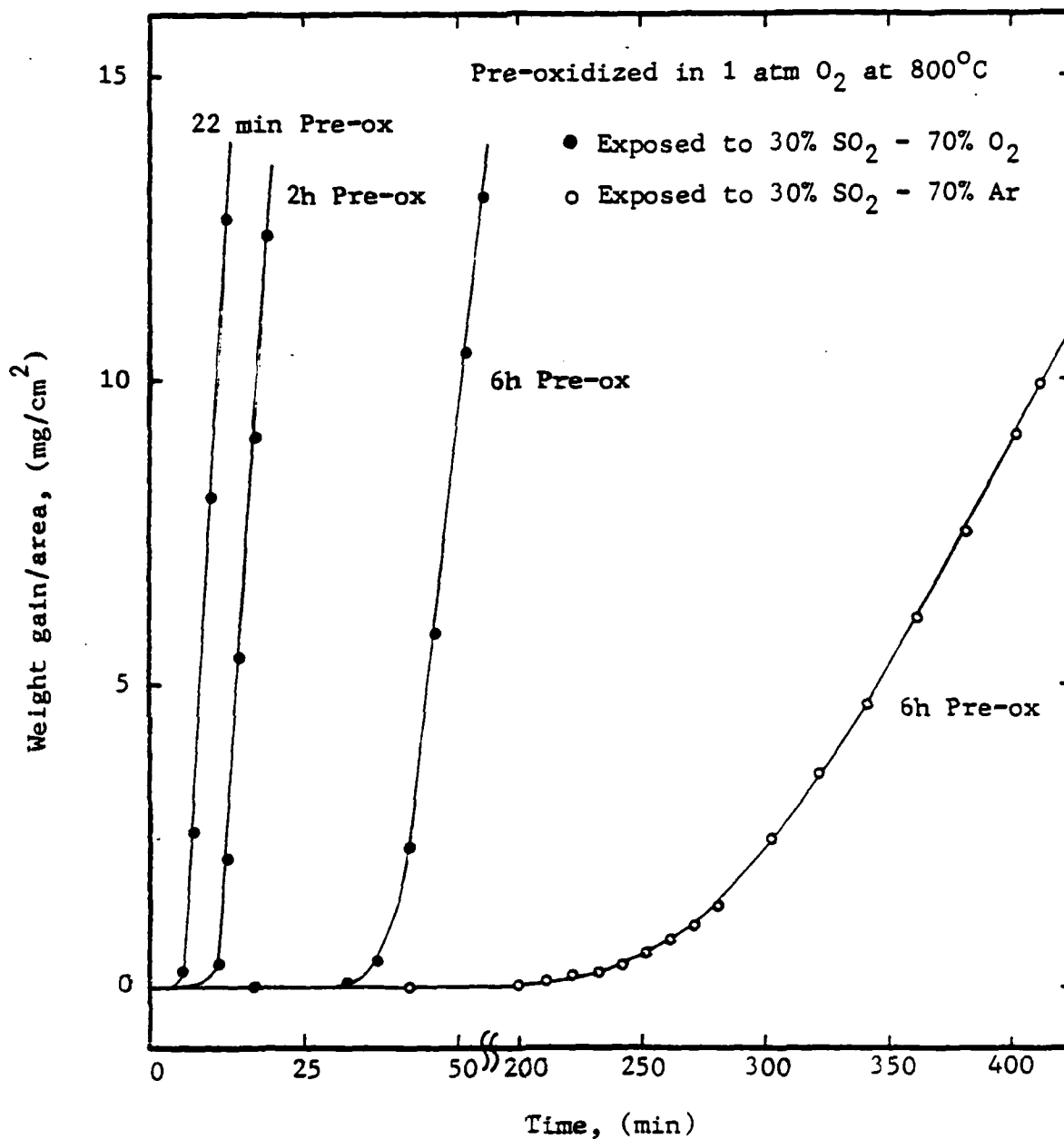
SCALE THICKNESS AS A FUNCTION OF TIME

FIGURE 7. Inner sulfide and outer nickel oxide scale thickness as a function of time.



WEIGHT GAIN VS TIME FOR NICKEL AT 800°C

FIGURE 8. Kinetics in 30% SO₂-variable O₂-balance Ar at 800°C. Note the initial trend for 2, 5 and 10% O₂ and the behavior for ≥ 20% O₂.



Weight gain after exposure to the Gas Mixtures at 800°C

FIGURE 9. Effect of Pre-oxidation in pure O₂ on corrosion of nickel in SO₂-O₂ gas mixtures. Samples exposed to 1 atm O₂ at 800°C.

TIME (Min.)	APPROX. Nio Thickness (μm)
22	1.6
120	6
360	7.4
360	7.9

FIGURE 10.

Comparison of theory (solid lines) with experimental data for isothermal ionic conductivity in yttria-stabilized zirconia as a function of vacancy concentration.

Experimental Data:

- ▽ Dixon, et al. (1963) ref. (6)
- O Strickler and Carlson (1964) ref. (7)
- X Strickler and Carlson (1965) ref. (8)
- Bauerle and Hrizo (1969) ref. (9)
- Δ Cassleton (1970) ref. (10)
- Ioffe et al (1978) ref. (11)

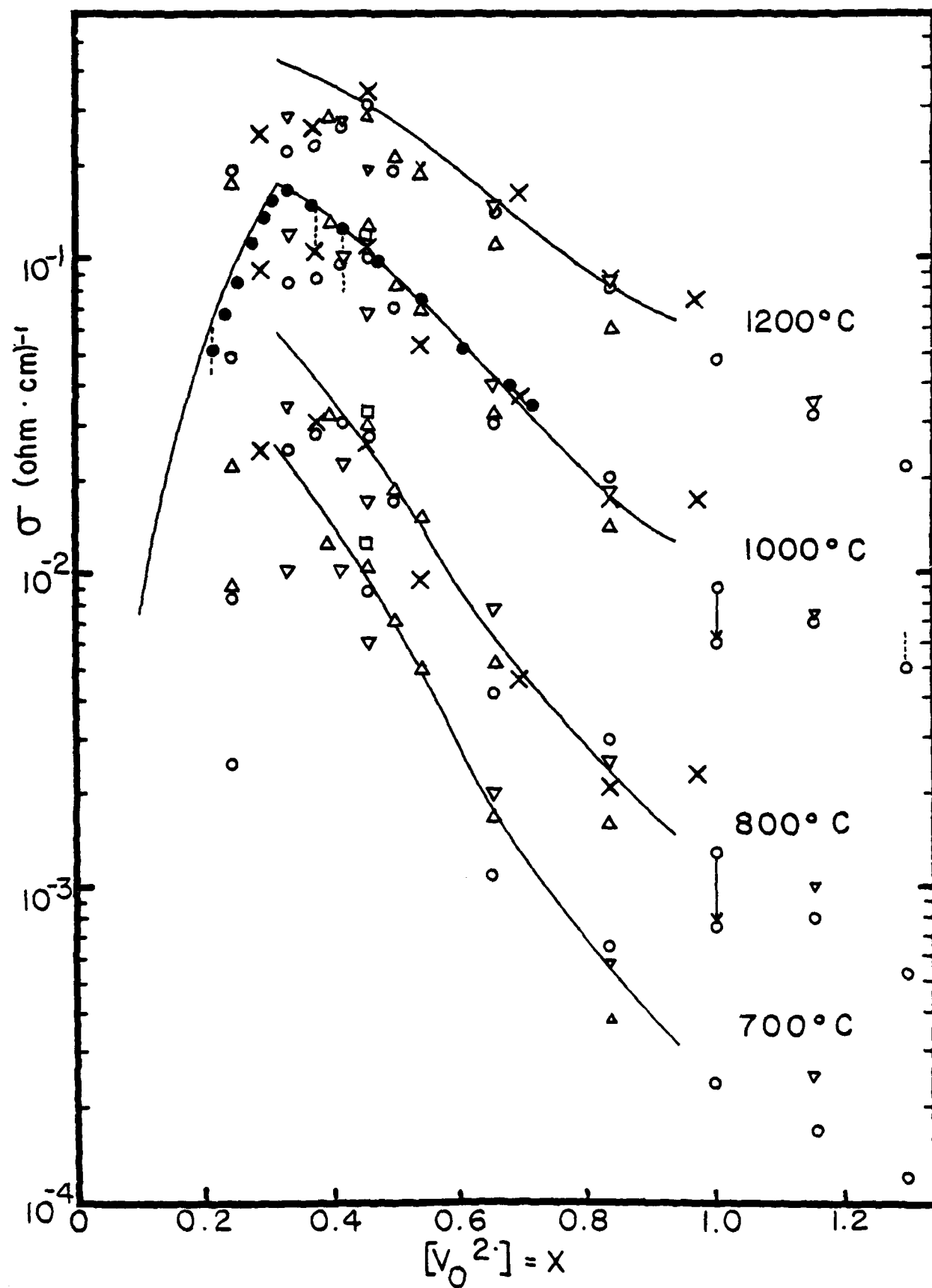
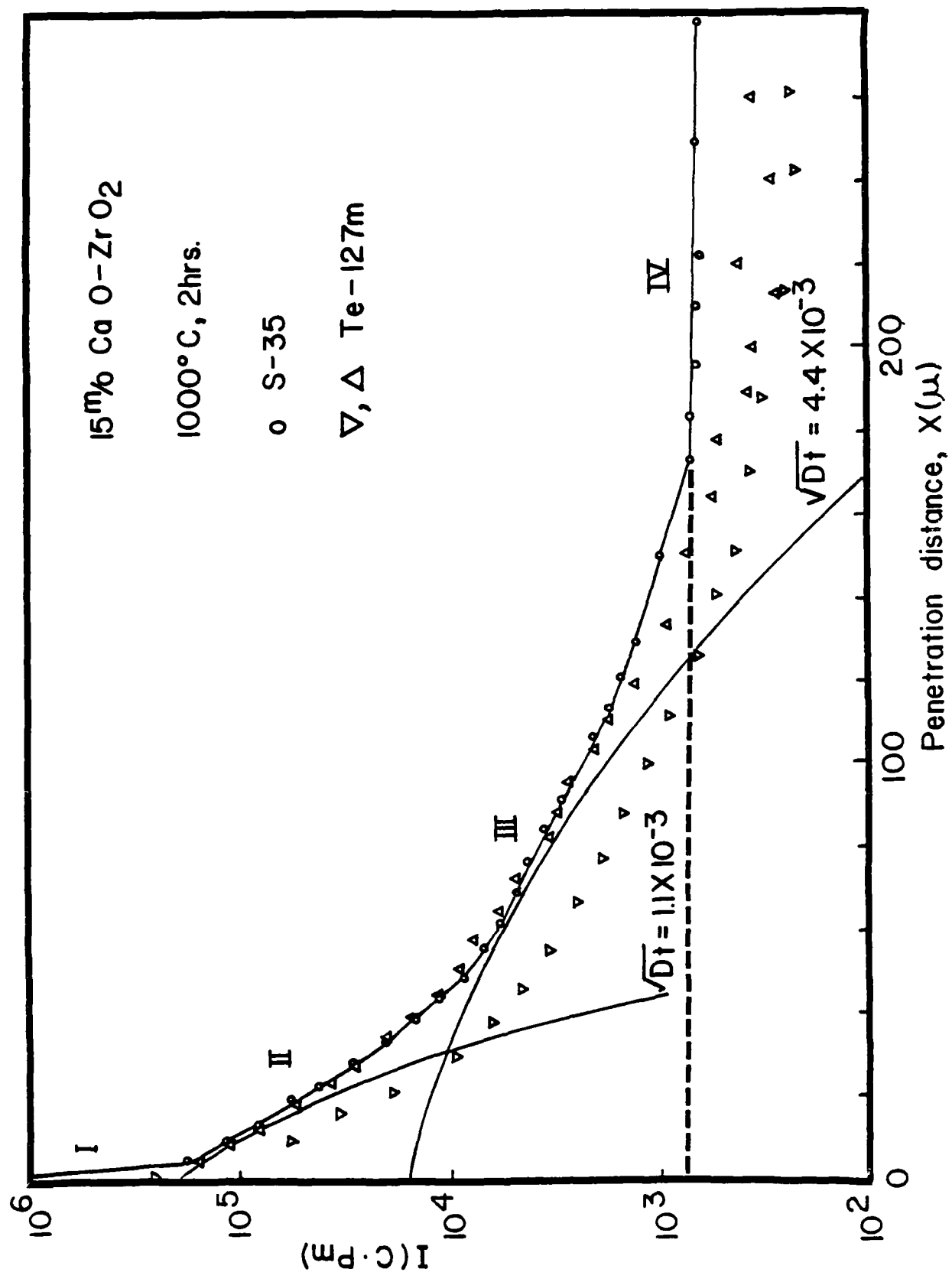


FIGURE 11.

Typical penetration profile for sulfur - 35 and
tellurium - 127m in calcia stabilized zirconia
(15 m/o CaO).



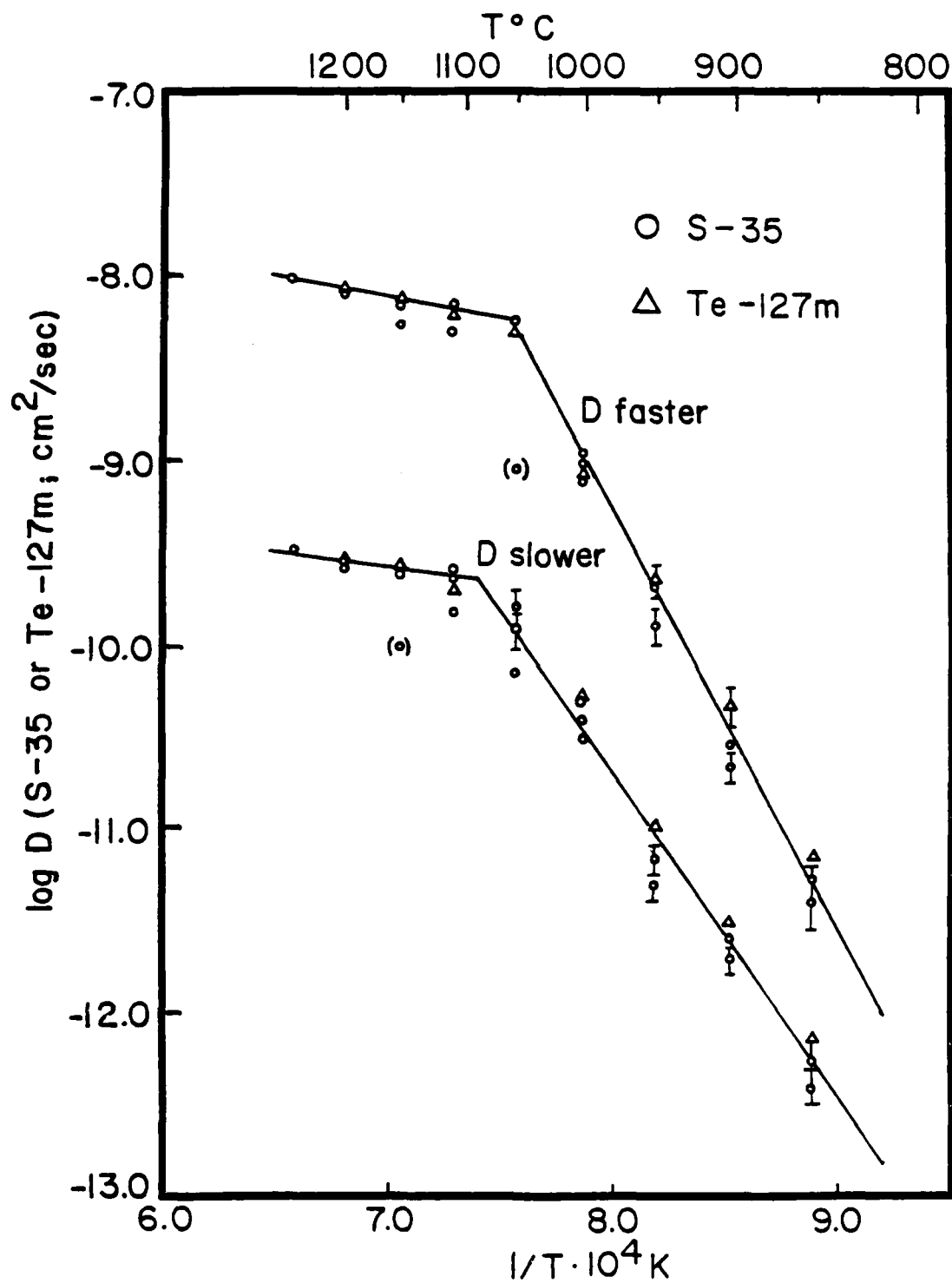


FIGURE 12. Arrhenius plots for D_s and D_f in calcia stabilized zirconia (15 m/o CaO)

VE
MED
8